

Gamma-ray Spectral Analysis of Three Energetic Millisecond Pulsars

Department of Physics, The University of Hong Kong, Pokfulam
Road, Hong Kong

Wang Wenchao

3030053350

Declaration

I hereby declare that this whole dissertation report is my own work, except the parts with due acknowledgment, and that it has not been previously included in a thesis, dissertation or report submitted to this University or to any other institution for a degree, diploma or other qualifications.

Signature: _____

Name: Wenchao Wang

Date: August 2018

Acknowledgments

Lots of people give me much precious help. First of all, I really appreciate my supervisor Dr. Stephen Chi Yung Ng for his great support, patience and kindness. Prof. Takata also provides me much help in term of pulsars' emission mechanisms and numerical simulations and is really charming. In addition, I thank Ms. Ruby Cho Wing Ng for her invaluable guidance and advice. They give me not only knowledge and techniques but also encouragements. Therefore, I would like to express my most sincere thanks to them.

Abstract

PSRs J0218+4232, B1821-24 and B1937+21 are among the most energetic and fastest-spinning millisecond pulsars (MSPs). They have been studied in all radio, X-ray and gamma-ray bands. The *Fermi* LAT Pass 8 data was published in 2015 and has lots of advantages over the old Pass 7 data, such as increased effective area and wider energy range. Since the recent gamma-ray spectral analysis of the three MSPs are relatively old, I redo the gamma-ray spectral analysis of the MSPs with four-year more *Fermi* LAT observational data and newly published Pass 8 data. I obtain better fit results for gamma-ray spectra of the three MSPs with smaller errors and larger test statistic values. I also do numerical simulations to test the two-layer model using the new observational data. By minimizing the differences between the predictions of the two-layer model and the real data, I fit the independent parameters of the two-layer model. I find that the simplified two-layer model can predict broadband spectra of the three MSPs which are very close to the observational data from *Fermi* LAT in most energy ranges.

Contents

Declaration	i
Acknowledgments	ii
Abstract	iii
List of Figures	vii
List of Tables	xi
1 Introduction	3
1.1 Neutron Stars and Pulsars	3
1.2 Emission Mechanism of Pulsars	4
1.2.1 Magnetic Dipole Model	5
1.2.2 Synchrotron Radiation	6
1.2.3 Inverse-Compton radiation	10
1.2.4 Curvature Radiation	14

1.3	Millisecond Pulsar	15
1.3.1	P- \dot{P} Diagram	15
1.3.2	Origin of Millisecond Pulsars	17
1.4	Introduction to the Three MSPs and Previous Works	18
1.5	Objectives	20
2	Gamma-Ray Analysis and Results	23
2.1	Introduction to the <i>Fermi Gamma-Ray Space Telescope</i>	23
2.2	A Brief Introduction to Fermi Data Analysis	26
2.3	<i>Fermi</i> LAT Data Analysis	29
2.3.1	Verifying the Data Analysis Process	30
2.4	PSR J0218+4232	31
2.4.1	Count Maps And Count Cubes	32
2.4.2	Binned Likelihood Analysis	34
2.5	PSR B1821-24	40
2.5.1	Count Maps And Count Cubes	40
2.5.2	Binned Likelihood Analysis	41
2.6	PSR B1937+21	45
2.6.1	Phase Averaged Analysis	45

2.6.2	Phase Resolved Analysis	52
2.7	Summary of the Results	58
3	Theory and Simulation	60
3.1	A Brief Introduction to the Outer Gap Model	60
3.2	Two-Layer Model	62
3.3	X-ray Emission Model	67
3.4	Simple Optimizations of Numerical Calculation	69
3.4.1	Accuracy	69
3.4.2	Speed of Computation	70
3.5	Numerical Calculation of Spectra Based on the Two-Layer Model	72
4	Discussion	77
4.1	Constraints of the Two-Layer Model	78
4.2	Inconsistency Between the Two-Layer Model and Fit Results	81
5	Conclusion and Future Works	82
5.1	Conclusion	82
5.2	Analysis With LAT 8-year Point Source List	83
5.3	Future Works	84

List of Figures

1.1	Spatial distribution of some pulsars in galactic coordinate system.	4
1.2	Braking indices of some pulsars.	6
1.3	Spectrum shape of synchrotron radiation for a single particle . .	8
1.4	Two photons collide with an electron. In the frame S' , two photons collide with a rest electron successively. In the frame S , the electron is no longer at rest and the positions of the two events are x_1 and x_2	10
1.5	Diagram of Inverse Compton Process.	14
1.6	Positions of pulsars in P- \dot{P} diagram.	16
1.7	A schematic diagram of Roche lobe.	18
1.8	Pulse profiles of PSR B1937+21 in radio, X-ray and gamma-ray bands. The figure is adopted from Ng et al. (2014)	20
2.1	The figure (https://www-glast.stanford.edu/instrument.html) illustrates how <i>Fermi</i> LAT tracks incident gamma-ray photons. .	24
2.2	The count maps of observational data and the spectral model. .	33

2.3	Three count maps from PSR J0218+4232's count cube.	33
2.4	The count map and residual map of PSR J0218+4232.	35
2.5	The log-log plot of flux to energy of PSR J0218+4232.	37
2.6	TS maps of PSR J0218+4232.	38
2.7	The count spectra and count residuals of PSR J0218+4232.	39
2.8	The count map of PSR B1821-24 (left) and the count map generated by the model (right).	40
2.9	Three count maps of PSR B1821-24's count cube.	41
2.10	The count map and residual map of PSR B1821-24 in linear scale.	42
2.11	The log-log plot of flux to energy of PSR B1821-24's gamma-ray spectrum.	42
2.12	TS maps of PSR B1821-24.	44
2.13	The count spectra and count residuals of PSR B1821-24.	44
2.14	The count maps of PSR B1937+21 created from observation data (left) and from the spectra model (right).	46
2.15	Three count maps of PSR B1937+21's count cube.	46
2.16	The count map created from observational data (left) and residual map (right) of PSR B1937+21.	47
2.17	TS maps of PSR B1937+21.	48
2.18	The count spectra and count residuals of the fitted spectral model.	49

2.19 Top panel is counts spectra for all sources within the ROI. Bottom panel shows the count residuals.	50
2.20 TS maps of PSR B1937+21 (power-law model).	51
2.21 The log-log plot of flux to energy of PSR B1937+21's gamma-ray spectrum.	51
2.22 Top left panel shows the pulse phase of PSR B1937+21 in gamma-ray band. The figure is produced by tempo2.	52
2.23 Light curves of PSR B1937+21 by different telescopes. The data and figure are from Guillemot et al. (2012)	53
2.24 The count maps of PSR B1937+21 created from observation data (left) and from the spectra model (right).	54
2.25 Three count maps extracted from PSR B1937+21's count cube.	55
2.26 The count maps of PSR B1937+21 created from observation data (left) and from the spectra model (right).	56
2.27 The count spectra (top) of all sources including those with only fixed parameters and count residuals (bottom) of the fit for PSR B1937+21.	56
2.28 PLEC model spectrum of PSR B1937+21 (phase resolved). . .	57
2.29 TS maps of PSR B1937+21.	58
3.1 Geometry and charge density distribution of the two-layer model.	63
3.2 The observed gamma-ray spectrum of PSR J0218+4232 compared with the two-layer model.	73

3.3	The gamma-ray spectrum of PSR B1821-24 by the two-layer model.	73
3.4	The gamma-ray spectrum of PSR B1937+21 by the two-layer model. (blue line)	74
3.5	The broadband spectrum of PSR J0218+4232.	75
3.6	Broadband spectrum of PSR B1821-24.	75
3.7	The broadband spectrum of PSR B1937+21.	76
4.1	Effects of f on the shape of the gamma-ray spectrum.	78
4.2	Effects of g_1 on the shape of the gamma-ray spectrum.	79
4.3	Effects of h_1/h_2 on the shape of the gamma-ray spectrum.	79
5.1	Gamma-ray spectra of PSR J0218+4232 with PLEC2 model.	85
5.2	Gamma-ray spectra of PSR B1821-24 with PLEC2 model.	85
5.3	Count spectra and residuals of PSR J0218+4232	86
5.4	Count spectra and residuals of PSR B1821-24.	86

List of Tables

1.1	Spin and derived properties of PSRs J0218+4232, B1821-24 and B1937+21.	21
1.2	Spectra properties of the three MSPs from previous studies. . .	21
2.1	The spectra fit results with data from 2008 August 4 to 2011 August 4.	31
2.2	Fit results with data from year 2009 to year 2018.	32
2.3	Numbers of photon counts of count maps in different energy bands for PSR J0218+4232.	34
2.4	Fit parameters of the spectra model of PSR J0218+4232. . . .	36
2.5	Fit parameters of the spectra model of PSR B1821-24.	43
2.6	Fit parameters of the spectra model of PSR B1937+21.	48
2.7	Photon index comparison of power-law model between different studies.	49
2.8	Fit parameters of the spectra model of PSR B1937+21 (phase resolved).	57

2.9	Fit parameters of the spectra model of PSR J0218+4232.	58
2.10	Fit results of power-law model for PSR B1937+21.	59
2.11	TS values comparison between the new results and the previous results for the three MSPs.	59
3.1	X-ray Properties of the PSRs J0218+4232, B1937 and B1821-24.	69
3.2	Flux densities of PSRs J0218+4232, B1937+21 and B1821-24.	69
3.3	The results of fit parameters for the three MSPs.	72
4.1	The best-fit parameters of the two-layer model and observa- tional properties for a few pulsars	80
5.1	Fit results of PSRs J0218+4232 and B1821-24 with LAT 8-year Point Source List.	84
5.2	TS values comparison between 3FGL (older) and FL8Y (newer) source list.	84

List of Tables

Chapter 1

Introduction

1.1 Neutron Stars and Pulsars

Neutron stars are produced by supernovae explosion of massive stars which have about four to eight solar mass. After a supernova explosion, a star leaves a central region. And the central region collapses because of the effect of gravity until protons and electrons combine to form neutrons ($e^- + p \rightarrow n + \nu_e$) —the reason why they are called “neutron stars”. Because neutrons have no electromagnetic force on each other, they can be squeezed very tightly. Therefore, a neutron star has a tremendous high density (about $5 \times 10^{17} \text{ kg/m}^3$) and its diameter and mass are about 20km and 1.4 solar mass respectively. What prevents a neutron star to continue to contract is the degeneracy pressure of neutrons.

Pulsars are fast-spinning neutron stars. They have rotational periods from a few milliseconds to several seconds. For example, the rotational period of PSR B1937+21 is about 1.56ms while PSR B1919+21 is approximately 1.34s. As we know, a star can be ripped by centrifugal force if the star rotates too fast.

We can estimate lower limits of density of a star with the equation $\rho = \frac{3\pi}{P^2 G}$, where P is the rotational period of a pulsar. Just for simplicity, let P be 1s. Then we get $\rho \approx 1.4 \times 10^{11} \text{ kg/m}^3$. With the knowledge that the density of a white dwarf is about $1 \times 10^9 \text{ kg/m}^3$ which is smaller than the lower density limit, the observed fast-spinning stars belong to the kind of stars which are much denser than white dwarfs. As a result, neutron stars are ideal candidates for pulsars.

More than 2000 pulsars have been discovered so far. Most of them are in the disk of our Galaxy while we also can find a small portion of them in high latitude, which can be seen clearly in Figure 1.1. This may because they cannot escape the gravitational potential if their kinetic energy is not large enough. Besides, even though they have large enough velocities to escape from their birth region, there are some probabilities that they become nearly non-detectable before reaching high latitude.

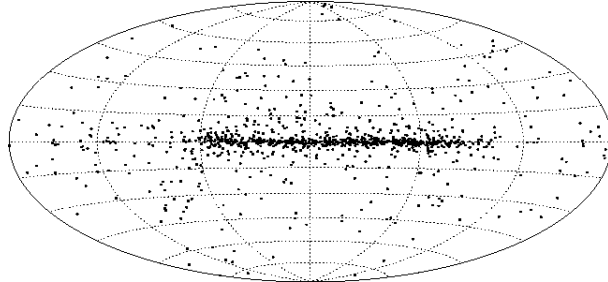


Figure 1.1: Spatial distribution of some pulsars in galactic coordinate system.

1.2 Emission Mechanism of Pulsars

Although the emission mechanism of pulsars has not been fully understood yet, some models have been developed trying to explain observational data. The following is a simple model that can explain some basic features of pulsars spectra. I will first introduce the magnetic dipole model, then the synchrotron

radiation and inverse Compton radiation.

1.2.1 Magnetic Dipole Model

Assuming a pulsar has a magnetic dipole moment \vec{m} , the angle between rotation axis and direction of \vec{m} is α , its angular velocity is Ω , radius is R and moment of inertia is I . Also assuming that energy of electromagnetic radiation is completely from the rotational energy, its spin-down rate can be written as:

$$\dot{\Omega} = -\frac{B_p^2 R^6 \Omega^3 \sin \alpha^3}{6c^3 I}$$

where B_p is magnetic field strength in the pole of the pulsar. Its surface magnetic field can also be estimated by:

$$B_s = \sqrt{\frac{3c^3 I}{2\pi^2 R^6} P \dot{P}} = 3.2 \times 10^{19} \sqrt{P \dot{P}}$$

where B_s is the strength of the surface magnetic field.

In general, a pulsar's spin-down rate can be expressed as $\dot{\Omega} = -K\Omega^n$, where K is a constant and n is called braking index. In magnetic dipole model n is three (Tong 999). Then the characteristic age of the pulsar can be defined as $P/2\dot{P}$ in the magnetic dipole model. For example, the Crab pulsar's rotation period is about $0.033s$ and period derivative is $4.22 \times 10^{-13}s/s$. The characteristic age is about 1200 years. The pulsar is a remnant of a supernova which is observed by ancient astronomers in 1054 AD, so the record shows that characteristic age can give us an order of magnitude estimate of a pulsar's real age.

Although the braking index is 3 in the magnetic dipole model, most of the pulsars' braking index is less than 3 as shown in Figure 1.2. The reason is that if a pulsar's spin down is completely determined by pulsar winds, the braking

index is one. Thus, the real braking index should be a combination of 1 and 3, which is usually less than three (Hamil et al. 2015).

Pulsar	n_{obs}	Ω s^{-1}	$\dot{\Omega}$ 10^{-10}s^{-2}
PSR B0531+21 (Crab)	2.51 ± 0.01	30.22543701	-3.862283
PSR B0540-69	2.14 ± 0.01	19.8344965	-1.88383
PSR B0833-45 (Vela)	1.4 ± 0.2	11.2	-0.157
PSR B1509-58	2.839 ± 0.001	6.633598804	-0.675801754
PSR J1846-0258	2.16 ± 0.13	3.0621185502	-0.6664350
PSR J1833-1034	1.857 ± 0.001	16.159357	-0.5275017
PSR J1119-6127	2.684 ± 0.001	2.4512027814	0.2415507
PSR J1734-3333	0.9 ± 0.2	0.855182765	-0.0166702

Figure 1.2: Braking indices of some pulsars.

1.2.2 Synchrotron Radiation

Synchrotron radiation is a special case of cyclotron radiation when a particle's speed is comparable to the speed of light. Because of the relativistic beaming effect, a very short radiation pulse can be observed when speeds of particles are large. I only aim to analyze the spectral properties of MSPs, so I focus on the spectrum property of synchrotron radiation. With Larmor's Formula we can derive the synchrotron radiation power of an electron:

$$P = \frac{2e^4\gamma^2\beta^2B_\perp^2}{3m_e^2c^3}, \quad (1.1)$$

where γ is the Lorentz factor of the electron, $\beta = v/c$ and B_\perp is the strength of magnetic field perpendicular to the circular motion plane. When $\beta \sim 1$, Function 1.1 can be simplified as:

$$P = \frac{2}{3}\frac{e^2c}{R^2}\gamma^4, \quad (1.2)$$

where $R = E/eB_\perp$ is the radius of the electron's circular motion. Furthermore, the power spectrum of a single electron can be described by Function 1.3

$$\begin{aligned} P(\nu) &= \frac{\sqrt{3}e^3 B \sin \alpha}{mc^2} \left(\frac{\nu}{\nu_c} \right) \int_{\nu/\nu_c}^{\infty} K_{5/3}(\eta) d\eta \\ &= \frac{\sqrt{3}e^2}{m_e R} \gamma \left(\frac{\nu}{\nu_c} \right) \int_{\nu/\nu_c}^{\infty} K_{5/3}(\eta) d\eta, \end{aligned} \quad (1.3)$$

where ν_c is the critical frequency and $K_{5/3}$ is modified Bessel function. The critical frequency can be expressed by Function 1.4

$$\begin{aligned} \nu_c &= \frac{3}{2} \gamma^2 \nu_{cyc} \sin \alpha \\ &= \frac{3}{4\pi} \frac{c}{R} \gamma^3, \end{aligned} \quad (1.4)$$

where α is the pitch angle and the ν_{cyc} is the frequency of corresponding cyclotron radiation. These functions do not give us very much information because of the integration of the modified Bessel function. We let $x = \nu/\nu_c$ and fix the environment variables such as magnetic field (B), Function 1.3 becomes:

$$P(\nu) = C \times x \int_x^{\infty} K_{5/3}(\eta) d\eta, \quad (1.5)$$

where C is a constant dependent on B . Thus, in order to analyze the power spectrum of synchrotron radiation, we only concentrate on the later part, which is

$$F(x) = x \int_x^{\infty} K_{5/3}(\eta) d\eta. \quad (1.6)$$

In reality, synchrotron radiation is not generated by a single particle. We describe the number density distribution of electrons with respect to energy by a single power-law model:

$$N(E) \approx CE^{-\delta}. \quad (1.7)$$

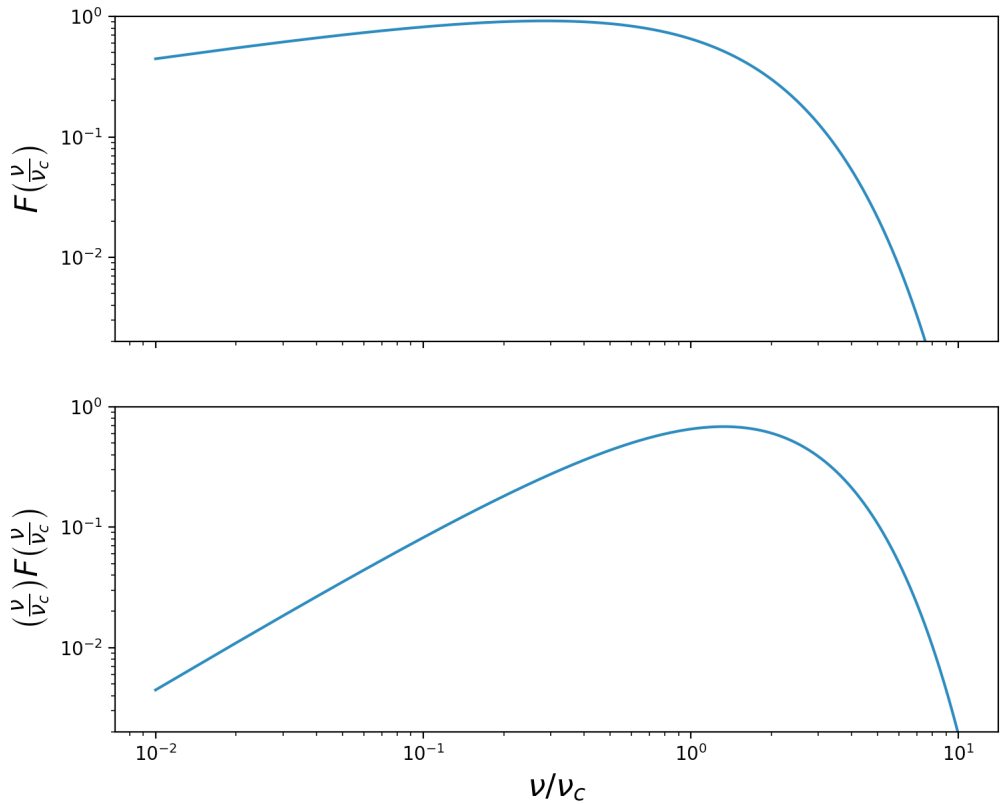


Figure 1.3: Spectrum shape of synchrotron radiation for a single particle (top). According to Equation 1.6, the top figure 1.6 describes the general shape of power spectrum of synchrotron radiation. When the frequency is larger than the critical frequency ν_c , the power goes down dramatically. However, the top figure does not show the information that at what frequency the charged particle emits the strongest power, which is revealed in the bottom figure. The bottom figure shows that most energy is emitted around the critical frequency.

For simplicity, we set the ambient magnetic field B to be a constant and make an approximation that all radiations are at a single frequency:

$$\nu \approx \gamma^2 \nu_{cyc}, \quad (1.8)$$

where the meaning of ν_{cyc} is the same as Function 1.4. Our objective is to know the relationship between total power of all electrons and their radiation frequency. We describe the relationship as Equation 1.9

$$-P(E)N(E)dE = Q_\nu d\nu \quad (1.9)$$

$$P(E) = \frac{4}{3}\sigma_T\beta^2\gamma^2cU_B, \quad (1.10)$$

where σ_T is electron Thompson scattering section, U_B is energy density of the environment magnetic field, Q_ν is the emission coefficient of synchrotron radiation and $E = \gamma m_e c^2$. With Equation 1.8, we have

$$P = \frac{dE}{d\nu} = \frac{m_e c^2}{2\sqrt{\nu\nu_{cyc}}}. \quad (1.11)$$

Combine Functions 1.11 and 1.9 we get:

$$Q_\nu = \frac{4}{3}\sigma_T\beta^2\gamma^2cU_B \frac{m_e c^2}{2\sqrt{\nu\nu_{cyc}}} N(E). \quad (1.12)$$

Ignoring constants in Function 1.9 we have

$$Q_\nu \propto \nu^{(1-\delta)/2}. \quad (1.13)$$

Function 1.13 shows that if the number density of electrons is a power-law distribution, the spectrum of synchrotron radiation is also a power-law model.

1.2.3 Inverse-Compton radiation

If an energetic relativistic photon collides with a charged particle from a proper incident angle, the photon's energy decreases and its direction changes. This is the process of Compton Scattering. Inverse-Compton radiation is the opposite process and a low energy photon gained energy from an ultra-relativistic electron in the process.

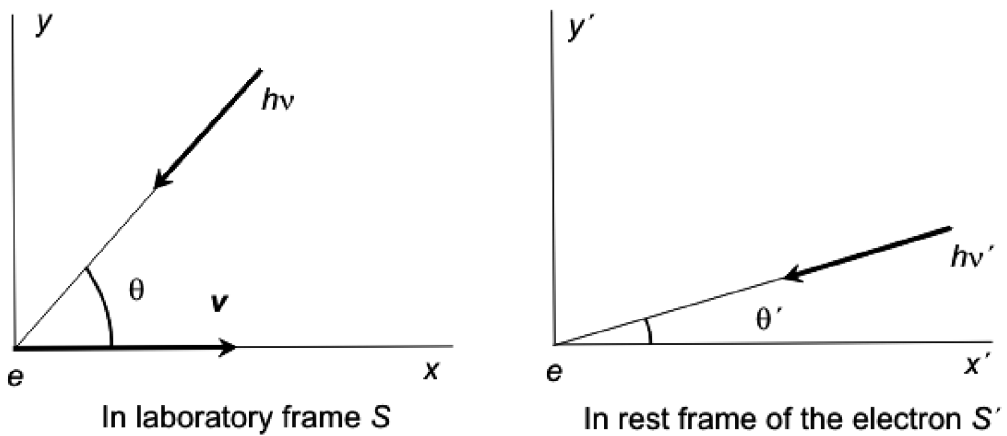


Figure 1.4: Two photons collide with an electron. In the frame S' , two photons collide with a rest electron successively. In the frame S , the electron is no longer at rest and the positions of the two events are x_1 and x_2

As Figure 1.4 shows, in the laboratory frame (S), the incident angle and energy of a photon is θ and $h\nu$ respectively. The speed of the electron is v . In the electron rest frame (S'), we change the denotation to θ' and $h\nu'$. Also, let the position of the electron be the origin point of S' . We can study the whole process in the S' frame, then transfer the result to the S frame by Lorentz transformation.

In the S' frame, the electron is at rest, so its energy is $m_e c^2$. For Inverse Compton scattering, the energy of an incident photon (less than several keV) is much less than the rest energy of an electron (about 0.51 MeV) and the relationship can be expressed by $h\nu' \ll m_e c^2$. Therefore, this can be treated

as Thompson Scattering process. Let the Poynting vector of incident photons be \vec{S}' and their energy density be U'_{rad} , we have equation 1.14

$$\vec{S}' = cU'_{rad}. \quad (1.14)$$

The electron absorbs the energy of the incident photons and then is accelerated. Thus, the accelerated electron will emit part of the energy taken from the incoming photon and the power of scattered radiation is denoted as P' . The ratio can be described by Thompson Scattering cross section σ_T which is:

$$\sigma_T = \frac{8\pi}{3} \left(\frac{e^2}{m_e c^2} \right)^2, \quad (1.15)$$

and the relationship between the electron radiation power and incoming photon energy flux can be described by Equation 1.16

$$P' = |\vec{S}'| \sigma_T, \quad (1.16)$$

Combine Equations 1.14 and 1.16, the radiation power emitted by the electron is:

$$P' = c\sigma_T U'_{rad}. \quad (1.17)$$

Then we need to find the relationship between the two frames S and S' . It mainly contains two parts: the relationship between P , P' and U_{rad} , U'_{rad} . Since $P = dE/dt$ and it is Lorentz invariant in inertial frame, we get the equation:

$$P = P'. \quad (1.18)$$

Now we hope to write U'_{rad} in terms of U_{rad} . U_{rad} is comprised by energy of a single photon and photon density. In the following analysis, all the denotations are correspondent to Equation 1.4. According to the relativistic Doppler shift

formula, we have:

$$h\nu' = (h\nu) \gamma (1 + \beta \cos \theta), \quad (1.19)$$

where $\beta = v/c$ and γ is Lorentz factor of an ultra-relativistic electron. Then we calculate the photon density. In the frame S' , the photon density is inverse proportional to the time interval (Δt) between the two photons striking the electron since total number of photons is Lorentz invariant. In laboratory frame S , we consider two photons collide with the electron at the 4-dimension vector of $(x_1, 0, 0, t_1)$ and $(x_2, 0, 0, t_2)$. According to the Lorentz transformation between inertial frames:

$$\left\{ \begin{array}{l} x = \gamma (x' + \beta ct') \\ y = y' \\ z = z' \\ t = \gamma \left(t' + \frac{\beta x'}{c} \right), \end{array} \right. \quad (1.20)$$

and because we set $x' = 0$, from Equation 1.20, the two events of two successive photons collide with the electron can be expressed as: $(\gamma vt'_1, 0, 0, \gamma t'_1)$ and $(\gamma vt'_2, 0, 0, \gamma t'_2)$. As Figure 1.5 shows, the time interval of two successive photons (reciprocal of frequency) in frame S is:

$$\begin{aligned} \Delta t &= (t_2 - t_1) + \frac{(x_2 - x_1) \cos \theta}{c} \\ &= \gamma(t'_2 - t'_1) + \frac{\gamma v (t'_2 - t'_1) \cos \theta}{c} \\ &= \Delta t' \gamma (1 + \beta \cos \theta). \end{aligned} \quad (1.21)$$

Equation 1.21 shows that the relationship of photon number density between frame S and S' is:

$$n' = n \gamma (1 + \beta \cos \theta). \quad (1.22)$$

Combine Equations 1.22 and 1.19 we can transfer the incident photon energy density from frame S to S' according to Equation 1.23

$$U'_{rad} = U_{rad} [\gamma (1 + \beta \cos \theta)]^2. \quad (1.23)$$

In Equation 1.23, the incoming photon energy density is a function of the incident angle (θ), in order to get the total photon energy density, we integrate the equation over θ . Then we get:

$$U'_{rad} = \frac{4}{3} U_{rad} \left(\gamma^2 - \frac{1}{4} \right). \quad (1.24)$$

Combine Equations 1.24 and 1.17, the total scattered radiation power is:

$$\begin{aligned} P' &= P \\ &= \frac{4}{3} \sigma_T c U_{rad} \left(\gamma^2 - \frac{1}{4} \right). \end{aligned} \quad (1.25)$$

As mentioned before, P' and P are the total radiation powers after scattering. Before the low energy photons gain energy, they give away some energy first which is $\sigma_T c U_{rad}$. Therefore, we have to subtract this value from Equation 1.25 to calculate the rate of net energy gain, which is described by Equation 1.26.

$$\begin{aligned} P' = P = \frac{dE}{dt} &= \frac{4}{3} \sigma_T c U_{rad} \left(\gamma^2 - \frac{1}{4} \right) - \sigma_T c U_{rad} \\ &= \frac{4}{3} \sigma_T c U_{rad} \beta^2 \gamma^2. \end{aligned} \quad (1.26)$$

If we compare Equation 1.26 with Equation 1.11, we find that the form is very similar between these two equations.

$$\frac{P_{IC}}{P_{sync}} = \frac{U_{rad}}{U_B}, \quad (1.27)$$

where U_B is the energy density of environment magnetic field.

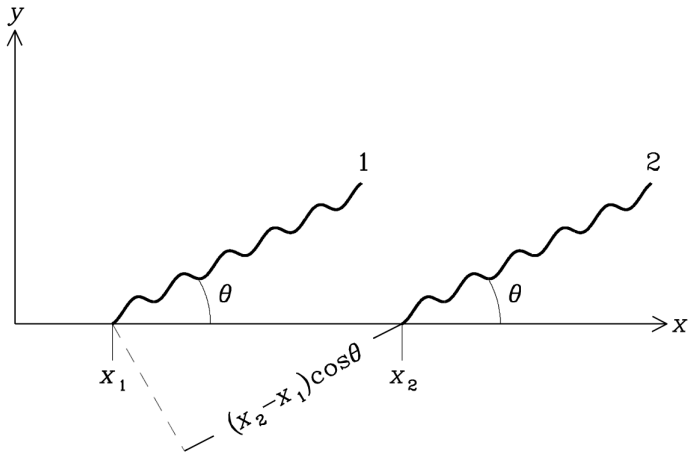


Figure 1.5: Diagram of Inverse Compton Process.

1.2.4 Curvature Radiation

Curvature radiation is the main source of gamma-ray photons. Charged particles not only move around magnetic field lines (synchrotron radiation), but also along magnetic field lines (curvature radiation) because the magnetic field is very strong.

Equation 1.1 shows that total synchrotron radiation power is related to pitch angle (because of the term B_\perp), and if the pitch angle is 0, there will be no synchrotron radiation. However, curvature radiation can still be generated and is dependent on the curvature radii of magnetic field lines:

$$P = \frac{2}{3} \frac{e^2 c}{s^2} \gamma^4, \quad (1.28)$$

where s is the curvature radii of magnetic field lines. Equation 1.28 is very similar to Equation 1.2 and the only difference is that R is changed to s .

Similarly, according to the Equation 1.3, the power spectrum of curvature radiation can be written as:

$$P = \frac{\sqrt{3}e^2}{m_e s} \gamma \left(\frac{\nu}{\nu_c} \right) \int_{\nu/\nu_c}^{\infty} K_{5/3}(\eta) d\eta, \quad (1.29)$$

where ν_c is the critical frequencies of curvature photons and equals to:

$$\nu_c = \frac{3}{4\pi} \frac{c}{s} \gamma^3. \quad (1.30)$$

According to Equations 1.28, 1.29 and 1.30, the spectral properties of curvature radiation are similar to synchrotron radiation. The only differences in the equations are particles' Lorentz factors and curvature radii.

1.3 Millisecond Pulsar

1.3.1 $P-\dot{P}$ Diagram

$P-\dot{P}$ diagram is an important tool for analyzing evolutions of pulsars. Period (P) and time derivative of period (\dot{P}) are two of pulsars' important characteristics. Analyzing the position of a pulsar in the $P-\dot{P}$ diagram can give us some valuable information such as what evolution stage the pulsar is in or the type of the pulsar, etc. Figure 1.6 is an example of a $P-\dot{P}$ diagram. The horizontal axis is pulsars' rotation periods and the vertical axis is first time derivative of rotation periods (\dot{P}). In this $P-\dot{P}$ diagram, the negative slope lines represent the strengths of surface magnetic fields while the positive slope lines represent the characteristic ages of pulsars. The following is a short explanation for this. From previous discussion, we have known that the characteristic age of a pulsar is $\tau = -P/\dot{P} = P/(-\dot{P})$, so line of constant τ is a set of straight lines with

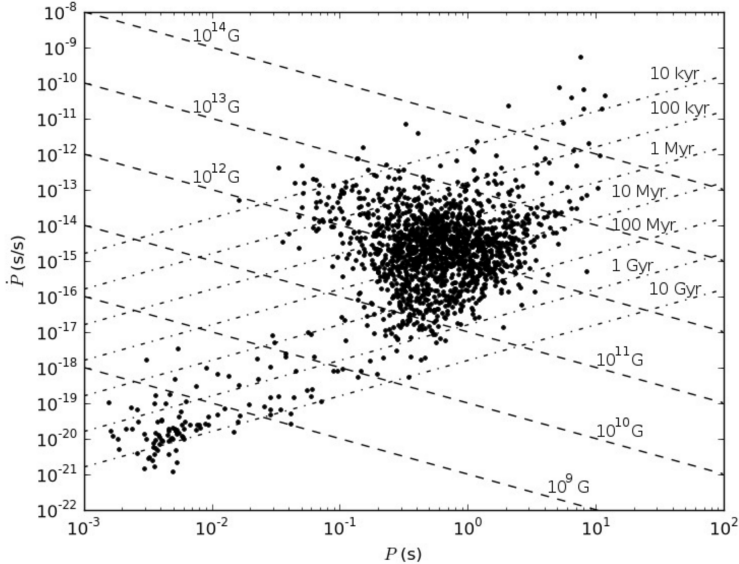


Figure 1.6: Positions of pulsars in $P\text{-}\dot{P}$ diagram.

equal positive slope. Since $B \propto \sqrt{P\dot{P}}$ the negative lines represent strengths of surface magnetic fields.

Figure 1.6 shows that most pulsars lie in the position of about 1s, 10^{-14}s/s . At the same time, a couple of stars lie at the bottom-left of Figure 1.6 — these are millisecond pulsars (MSPs). Their rotation periods are about 1-20 milliseconds. It is believed that MSPs are spun up by accretion of mass from their companion stars. In the above $P\text{-}\dot{P}$ diagram, we can observe that millisecond pulsars' surface magnetic fields are about three to four orders of magnitude lower than those of normal pulsars. However, an MSP has a relative strong magnetic field near its light cylinder (B_{lc}). For instance, PSR J1939+2134's B_{lc} is about 1.02×10^5 which is larger than Crab pulsar (9.55×10^5).¹ The reason is that an MSP's radius of light cylinder ($R_{lc} = c/\omega$) is much smaller than a normal pulsar's because of its short rotation period and the magnetic field near light cylinder can be estimated as $B_{lc} \sim (R/R_{lc})^3$. At the same time, pulsars' emission mechanism is closely related to their magnetic field near the

¹<http://www.atnf.csiro.au/research/pulsar/psrcat/>

light cylinder. As a result, like a normal pulsar, an MSP also can have a broadband spectrum from radio to gamma rays.

1.3.2 Origin of Millisecond Pulsars

From pulsars' emission mechanisms, we know that the magnetic field of a pulsar decreases with time while the spin period increases with time. But MSPs' spin periods are much shorter than normal pulsars and surface magnetic fields are a lot weaker. This makes an MSP seem to be both young and old. As a result, people think millisecond pulsars are old pulsars spun up by their companions. The companion stars transfer mass and angular momentum to accelerate the rotation speed of pulsar. Therefore, the aged pulsar can spin faster gradually.

Mass Transfer And Accretion In Binary Systems

X-ray binaries are a type of binary systems that is luminous in X-ray band. There are several kinds of X-ray binaries including low mass X-ray binaries (LMXB) and high mass X-ray binaries (HMXB). The mechanism of transferring mass is different in these two types of systems. Before discussing mass transfers, I will introduce Roche Lobe briefly. Figure 1.7 is a schematic diagram of Roche Lobe. We call two stars in an LMXB as A and B respectively for convenience. It is obvious that if an object is close to star A, the gravitational influence of A is so strong that the gravitational effect of the star B can be ignored. Similarly, this is true for star B. As a result, there must be a point where the effect of star A is equal to star B which is called inner Lagrange point. The two parts inside the largest equipotential lines of A and B are called Roche lobe. If star B crosses its Roche lobe, then its mass will be attracted by A, thus mass transfer between A and B happens. This is the main

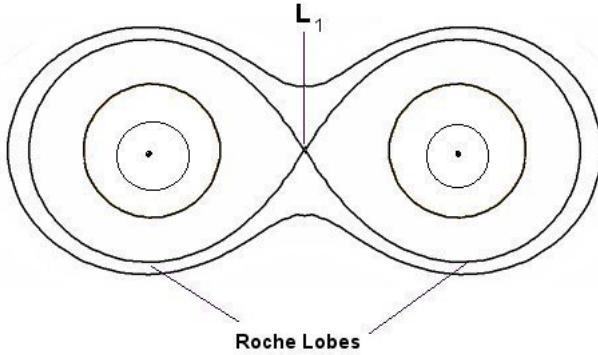


Figure 1.7: A schematic diagram of Roche lobe. L_1 is called inner Lagrange point which is the intersection of equipotential lines of the two stars.

way of mass transfer in LMXB. While in HMXB, the mass can be transferred by strong winds of the massive companion star.

The process of mass transfer can change the distance between two companion stars. If a low-mass star transfers mass to a high-mass companion star, the orbital separation will become larger. This can actually stop the mass transfer process and is a negative feedback. On the contrary, mass transfers from high-mass star to low-mass star will shrink the orbital distance.

1.4 Introduction to the Three MSPs and Previous Works

PSR B1937+21 is second fast spinning millisecond pulsar whose rotation period is about 1.56ms and was discovered in 1982 (Backer & et al. 1982), which makes it be the first discovered MSP. It has extremely strong magnetic field at the light cylinder with about 10^6 gauss, which is larger than Crab pulsar. Its basic properties are listed in Table 1.1. It has a double-peak pulse profile and the main pulse is much stronger than the other (Cusumano & et al. 2003). It

has very sharp pulsations and nearly 100% pulsed fractions.

Its gamma-ray properties were studied using *Fermi* LAT and its spectra were fitted by both a simple power-law model and a power-law with exponential cutoff (PLEC) model with photon-index of 2.38 ± 0.07 and 2.1 ± 0.2 respectively. However, the researchers report that the simple power-law model is preferred according to the convention in Abdo et al. (2013) (Ng et al. 2014). In X-ray energy band, PSR B1937+21 has been observed with *XMM-Newton* and *NuSTAR* (Ng et al. 2014; Gotthelf & Bogdanov 2017).

PSR B1821-24 is in the globular cluster M28. There are about a dozen pulsars discovered in M28, and PSR B1821-24 is the brightest one. In addition, PSR B1821-24 is the most energetic MSP discovered whose spin-down luminosity is about 2.2×10^{36} erg s $^{-1}$. Like PSR B1937+21, it has two very narrow pulses and the duty cycle is only about a few percent (Jenet et al. 2005).

The gamma-ray spectrum of PSR B1821-24 is fitted by a PLEC model with a photon index of 1.6 ± 0.3 using 44 months of *Fermi* LAT data (Johnson et al. 2013). *NuSTAR* observed the globular cluster M28 in June 2015. Though *NuSTAR*'s clock drift makes it hard to resolve the rotation period of PSR B1821-24, researchers have invented a method to correct the photon arrival times (Gotthelf & Bogdanov 2017).

PSR J0218+4232 is also a very energetic MSP with a spin-down luminosity of 2.4×10^{35} erg s $^{-1}$. Unlike the PSRs B1937+21 and B1821-24 which are solitary, it is accompanied by a white dwarf with an orbital period of two days at a distance of about 3.15 kpc (Verbunt et al. 2003). It was also studied using *Fermi* LAT and its spectrum is fitted by a PLEC model whose photon index is 2.0 ± 0.1 (Abdo et al. 2013).

All three MSPs are very energetic and have very strong magnetic field at the light cylinders as Table 1.1 shows, which makes them can be observed in radio, X-ray and gamma-ray bands like young pulsars. Additionally, they show aligned pulse profiles in radio, X-ray and gamma-ray bands as Figure 1.8 shows. This may implies a different emission mechanism that radio, X-ray and gamma-ray emission is from the same location in a pulsar's magnetosphere. The gamma-ray spectral properties of the three MSPs are listed in Table 1.2.

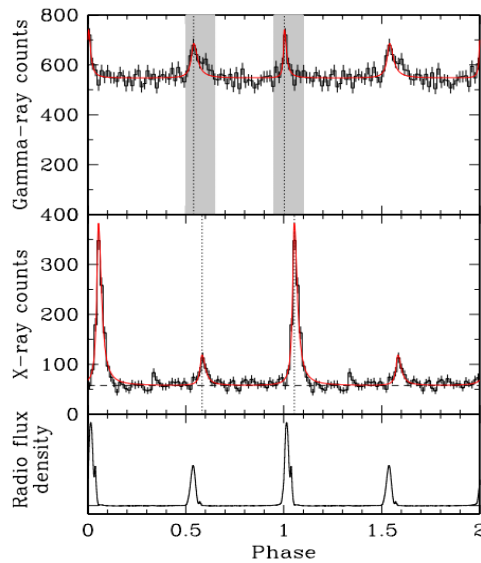


Figure 1.8: Pulse profiles of PSR B1937+21 in radio, X-ray and gamma-ray bands. The figure is adopted from Ng et al. (2014)

1.5 Objectives

Many gamma-ray studies about the three MSPs are a little bit old and now we have about a lot more *Fermi* LAT data. Besides, in 2015, Fermi team released Pass 8 data including many improvements, such as better energy measurement and significantly improved effective area. Additionally, there are new hard X-ray studies of the three MSPs using *NuSTAR* which provide better X-ray

²<http://www.atnf.csiro.au/research/pulsar/psrcat/>

	J0218+4232	B1821-24	B1937+21
Distance (kpc)	3.15	5.50	3.50
Period (ms)	2.32	3.05	1.56
Period Derivative (\dot{P} , 10^{-20})	7.74	162	10.5
Spin Down Age (10^8 yr)	4.76	29.9	2.35
Surface Magnetic Field (10^8 G)	4.29	22.5	4.09
Light Cylinder Magnetic Field (10^5 G)	3.21	7.40	10.2
Spin Down Energy (\dot{E} , 10^{35} erg s $^{-1}$)	2.4	22	11

Table 1.1: Spin and derived properties of PSRs J0218+4232, B1821-24 and B1937+21. The data are from the ATNF Pulsar Catalogue ²

	J0218+4232	B1821-24	B1937+21
Energy Range (GeV)	$0.1 \sim 100$	$0.1 \sim 100$	$0.5 \sim 6$
Photon Index Γ	2.0 ± 0.1	1.6 ± 0.3	1.43 ± 0.87
Cutoff Energy (GeV)	4.6 ± 1.2	3.3 ± 1.5	1.15 ± 0.74
Photon Flux (10^{-8} cm $^{-2}$ s $^{-1}$)	7.7 ± 0.7	1.5 ± 0.6	1.22 ± 0.23
Energy Flux (10^{-11} erg cm $^{-2}$ s $^{-1}$)	4.56 ± 0.24	1.3 ± 0.2	1.98 ± 0.32

Table 1.2: Spectra properties of the three MSPs from previous studies ³ (Ng et al. 2014; Guillemot et al. 2012).

measurements. As a result, it is time to redo the gamma-ray analysis with the newer dataset and more gamma-ray data in order to gain more precise results. In addition, we also plan to build a self-consistent emission model to explain the non-thermal high energy observations of the three MSPs.

Therefore, my main objective is to use the new data to redo the gamma-ray analysis of the three energetic MSPs mentioned above. Then, I will do a numerical simulation based on a theoretical model called two-layer model and test if the predictions of the model are consistent with the new observational data. And finally, based on numerical simulations of the two-layer emission model, I will generate broadband spectra (including hard X-ray band and gamma-ray band) for all three MSPs.

Chapter 2

Gamma-Ray Analysis and Results

As mentioned before, because of very short rotation periods, MSPs usually have very small light cylinders compared with normal pulsars. Therefore, the magnetic field strength at the light cylinders are comparable with young pulsars, especially for my target objects — PSRs J0218+4232, B1937+21 and B1821-24, which are among the fastest spinning and most energetic MSPs. Thus, as normal pulsars, the three MSPs have broadband emissions so it is intriguing to analyze the spectral properties of them in gamma-ray band.

2.1 Introduction to the *Fermi Gamma-Ray Space Telescope*

The *Fermi Gamma-Ray Space Telescope* was launched on June 11, 2008 and opened a new window of studying supermassive black-hole systems, pulsars and so on. Its original name was *Gamma-Ray Large Area Space Telescope*

(GLAST) and changed to *Fermi Gamma-Ray Space Telescope* in honor of the great scientist Enrico Fermi.

The *Fermi Gamma-Ray Space Telescope* contains two parts: Gamma-Ray Burst Monitor (GBM) and Large Area Telescope (LAT) and the latter is the main instrument which is at least 30 times more sensitive than all gamma-ray telescopes launched before. I only use LAT for my purposes. Thus, I focus on the LAT instrument, which contains four main subcomponents including trackers, calorimeters, anti-coincidence detectors and data acquisition systems. The reason why the telescope is designed in this way is that high-energy gamma-rays cannot be refracted by lens or mirrors. Therefore, the working principles of the *Fermi* LAT and other gamma-ray telescopes are completely different.

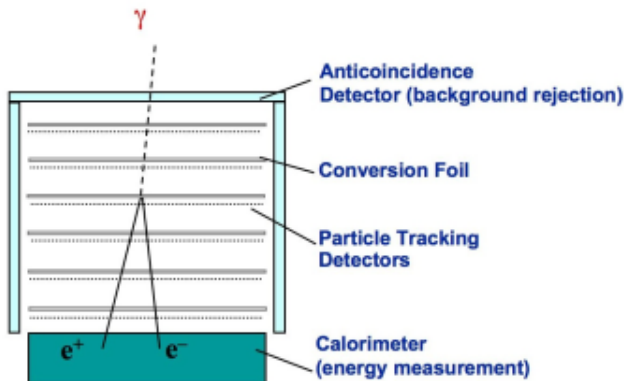


Figure 2.1: The figure (<https://www-glast.stanford.edu/instrument.html>) illustrates how *Fermi* LAT tracks incident gamma-ray photons.

Figure 2.1 demonstrates the very basic idea of the *Fermi* LAT working principles.

- Gamma-ray photons can enter the anti-coincidence detector freely while cosmic rays will generate signals which then tell the data acquisition system component to reject these particles. In this way, the *Fermi* LAT can distinguish the gamma-ray photons from high energy cosmic rays

with a confidence level over 99.9%.

- The conversion foil (Figure 2.1) can convert gamma-ray photons into electron and positron pairs. This procedure makes it possible to determine the directions of the incident gamma-ray photons.
- The tracker (particle tracking detectors in Figure 2.1) records the positions of the electrons and positrons generated from the gamma-ray photons. There are many trackers so the paths of particles can be constructed by numerical simulations.
- When the electrons and positrons reach the calorimeter, their energies can be measured. By calculating the energy relationships between the gamma-ray photons and the corresponding electrons and positrons, the energies of the original gamma-ray photons can also be obtained.
- The data acquisition system is like a filter of gamma-ray photons which can reject unwanted particles such as cosmic rays. Also, photons come from the Earth’s atmosphere are also rejected.

For a telescope, the ability to measuring the directions and energies of incident photons is very crucial. From the above descriptions of the *Fermi* LAT working principles, we know that the precision of construction of particles’ paths heavily influences how well we measure the directions and energies of gamma-ray photons. And this process is greatly dependent on simulations and available Fermi datasets, which means that with the improvements of simulations and datasets, the precision and sensitivity of *Fermi* LAT can also be improved. The Pass 8 data have reprocessed the entire Fermi mission dataset, so the quality of the dataset is much better. This is the main reason why I redo the analysis of the three MSPs.

2.2 A Brief Introduction to Fermi Data Analysis

Processes of Doing Fermi Analysis

When doing *Fermi* LAT data analysis, I basically dealt with two parts. The first part is processing observational data and the second is generating photon distributions based on spectra models. Cleaning data is straightforward including data selection, data filtering with good time intervals (GTIs), generating count maps and so on. Generating model-based count maps and count cubes needs a little bit more efforts and mainly includes the following procedures.

Firstly, I need to generate a spectra model of all sources in our region of interest (ROI). The model basically describes how strong each source is in different energy bands and different positions. The initial parameters of the model are from Fermi database. I do not fit positions of both point sources and diffuse sources when doing the data analysis. However, the model alone is not very helpful and I have to know other information in order to simulate photon distributions discussed as the following.

Since I am going to compare my simulation with the observational data, I have to take the telescope status into account. For example, the effective area of the telescope decreases when away from the optical axis. In addition, inclination angles and observation time intervals have direct influences on the number of photon counts. In short, after I get the simulated photon distribution from a model, it is necessary to transfer the initial simulation into the real simulation by applying the telescope functions.

After obtaining the photon distributions and spectra simulations, I then do comparisons in order to get the maximum likelihood of the model. I can divide the total energy band into many smaller energy bins and denote the number of photon counts in observational data as n_i , so that $\sum_i n_i = N$, where N is the total number of photons in full energy range. The observed number of photon counts in *i*th bin is a Poisson distribution with a mean value of m_i . In fact, the value m_i is the expected number of photon counts from our spectra model. Therefore, the distribution for *i*th bin can be expressed by Equation 2.1, where $P_i(n_i)$ is the possibility of observing the n_i photon counts for the *i*th bin.

$$P_i(n_i) = \frac{e^{-m_i} m_i^{n_i}}{n_i!}. \quad (2.1)$$

As a result, it is not hard to generalize the possibility from each bin to all bins, just by multiplying the possibilities for different bins.

$$\begin{aligned} P_{total} &= \prod_i P_i(n_i) \\ &= e^{-\sum_i m_i} \prod_i \frac{m_i^{n_i}}{n_i!}. \end{aligned} \quad (2.2)$$

In Equation 2.2, n_i is directly from observational data so they usually cannot be changed during the binned likelihood analysis. However, by changing the model, the m_i can be altered. Hence, my aim is to tweak the spectra model in order to make the total possibility P_{total} as large as possible.

This is the basic idea and procedure of doing Fermi data analysis. After doing these, I go further such as testing how significant the targets are by creating TS maps. The thesis basically follows the procedures.

Before finishing this part, I should briefly introduce the basic idea of TS maps. TS value stands for Test Statistic value which can be expressed as Equation 2.3

$$TS = -2 \ln \frac{L_{max,0}}{L_{max,1}}, \quad (2.3)$$

where $L_{max,0}$ and $L_{max,1}$ are the maximum likelihood of models in which the target source is not included and included respectively. According to Equation 2.3, the larger the TS value is, the larger $L_{max,1}$ is, which means that the probability of existence of the target source is larger. In order to generate a TS map, I divide the whole map into many sub-grids. In each sub-grid, the “gtlike” algorithm basically does two things. The first procedure is calculating the maximum likelihood value directly based on the spectra model ($L_{max,0}$). Then it adds an imaginary point source in the sub-grid, fits the source and gets the maximum likelihood ($L_{max,1}$) value. Therefore, I get two maximum likelihood values. In the end, it calculate the TS value for the sub-grid according to Equation 2.3.

After calculating the TS values for all sub-grids, I generate a TS map just by rendering colors according to each grid’s TS value. By comparing TS values of all sub-grids in a TS map, I can determine where the target source is most likely to be and how large the probability is.

Generally speaking, for each source, I generate two TS maps with and without the target source respectively. Then I determine how likely my target source is observed by calculating the TS values and compare the two TS maps. For instance, if the data show the source is observed, then the value of each pixel of the TS map containing the source should be low because the probability of adding an imaginary point source is low. On the contrary, the TS values of the pixels around the position of the target source should be significantly higher than other positions in the TS map if the target source is deleted from

the fitted spectra model.

2.3 *Fermi* LAT Data Analysis

The basic idea of fitting spectral parameters is to make the count cube generated by the model be as similar to the observational data as possible. A count cube is just a combination of many count maps in different energy bands. For example, a dataset whose energy range is from 100MeV to 100GeV can be divided into 30 bins. I generate a count map in each energy bin, thus I have 30 count maps.

A count map is basically generated by the following steps. Firstly, choose a pixel of a certain size. Then check each photon's direction to determine if the photon is in this pixel. If it is in the pixel, the photon counts of the pixel will add one. Therefore, the more photons fall within the pixel, the more photon counts the pixel has, hence the brighter the pixel is. By doing the same thing for every pixel in the ROI, a count map is generated. A count map shows what has been observed intuitively and offers a very basic idea of if the desired data is processed rightly.

The calculation process can be summarized as follows. First of all, I have to generate a spectra model for every known source in the region of interest (ROI) based on the Fermi database. The database includes *LAT* four-year Point Source Catalog (3FGL), Galactic diffuse emission (gll_iem_v06.fits) and the isotropic emission (iso_P8R2_SOURCE_V6_v06.txt). Then I produce a count cube based on the model. Generally speaking, the differences of the count cubes between the model and observation is obvious. Then, the Fermi software adjusts the parameters to make the difference smaller. Until the errors are

acceptable, the software outputs the final fitted parameters of corresponding spectra models.

I use a power-law with exponential-cutoff (PLEC) model to fit the observational data and it is a special case of the power-law with super-exponential-cutoff (PLSuperExpCutoff) model. The spectra of PLSuperExpCutoff can be described by Equation 2.4:

$$\frac{dN}{dE} = N_0 \left(\frac{E}{E_0} \right)^{\gamma_1} \exp \left[- \left(\frac{E}{E_c} \right)^{\gamma_2} \right], \quad (2.4)$$

where N_0 is called prefactor, E_c is the cutoff energy and the E_0 is a scale parameter. PLEC model is the special case where $\gamma_2 = 1$. My aim is to fit the parameters N_0 , E_c and γ_1 to make the model be more consistent with the *Fermi* LAT observational data.

2.3.1 Verifying the Data Analysis Process

Before analyzing the observations of my target sources, it is reasonable to test if my procedures for data processing are right. In order to do so, I try to do analysis for two bright pulsars PSRs J0007+7303 and J0534+2200. The reason I choose these two pulsars is that according to previous studies, they are bright and easy to detect with a large TS value of 43388 and 102653 for J0007+7303 and J0534+2200 respectively (Abdo et al. 2013).

In the spectra fit process, I do not use the same fit parameters as the previous paper (for instance, the number of free parameters in the ROI is different), however, I get similar results in terms of spectral index. In Table 2.1, I used the observational data from 2009-01-01 to 2013-02-01 in order to try to be consistent with the old results (Abdo et al. 2013). In addition, I also

fit spectra with observational data up to 2018-02-01 and Pass 8 dataset to test how big improvement I can make with the new Fermi Pass 8 dataset and more observational data. The results of year 2018 data are shown in Table 2.2.

Tables 2.1 and 2.2 mainly show two pieces of information. Firstly, my procedures for dealing with observation data have no obvious problems, so basically I can trust fit results of my target sources. Secondly, the *Fermi* Pass 8 LAT Data has improved the accuracy a lot. For example, as Table 2.1 shows, the photon indexes are 1.30 ± 0.02 and 1.4 ± 0.1 , which shows that the errors reduce a lot. Additionally, the TS value is more than double as before.

	Test Results			Previous Results		
	Γ	E_c (MeV)	TS	Γ	E_c (MeV)	TS
J0007+7303	1.30 ± 0.02	2010 ± 85	96979	1.4 ± 0.1	4700 ± 200	43388
J0534+2200	2.07 ± 0.01	9880 ± 572	239015	1.9 ± 0.1	4200 ± 200	102653

Table 2.1: The spectra fit results with data from 2008 August 4 to 2011 August 4. In the thesis, in order to make data analysis more convenient, I use some pipeline scripts to deal with the observational data. The "Test Results" column is the results generated by using the pipeline scripts. The "Previous Results" column lists the corresponding spectral properties based on the previous studies (Abdo et al. 2013). According to the standard PLEC model (described in equation 2.4), Γ is photon index and E_c is cutoff energy.

2.4 PSR J0218+4232

The region of interest (ROI) is a circle with a radius of 20° and all parameters of sources which are 8° outside of the center are fixed. For sources within

	Γ	E_c (GeV)	TS Value
J0007+7303	1.34 ± 0.02	2.20 ± 0.67	210166
J0534+2200	2.01 ± 0.01	9.20 ± 0.37	449946

Table 2.2: Fit results with data from year 2009 to year 2018. The physical meanings of Γ and E_c are the same as Table 2.1

8° , initial values of parameters are the same as their default values according to *Fermi* LAT four-year Point Source Catalog . In this case, there are seven point sources which have free parameters. In Figure 2.2, the green circles represent those sources. There are some very bright sources which have no free parameters in the outer parts of the count map. The reason is that they are so far away from PSR J0218+4232 that *Fermi* LAT can distinguish if a photon comes from the target source or other outer sources. As a consequence, I do not need to fit any parameters for those outer sources and their spectral properties are from *Fermi* LAT four-year Point Source Catalog . However, it is a different case for the nearby sources and they have to be fitted with the model.

2.4.1 Count Maps And Count Cubes

The left panel of Figure 2.2 is the count map of PSR J0218+4232 created directly from the observational data. In the center of the left panel, the target source can be seen clearly. The dimensions of the figures seem to be weird and the reason why the count map is 141 pixels wide is that I need to select a circle region from the original data. However, when generating a count map, I have to assign the sizes for x and y axis separately, which means that a count map is actually rectangular. As a consequence, I have to crop a rectangular from the original circle region and usually, the rectangular is chosen as a square.

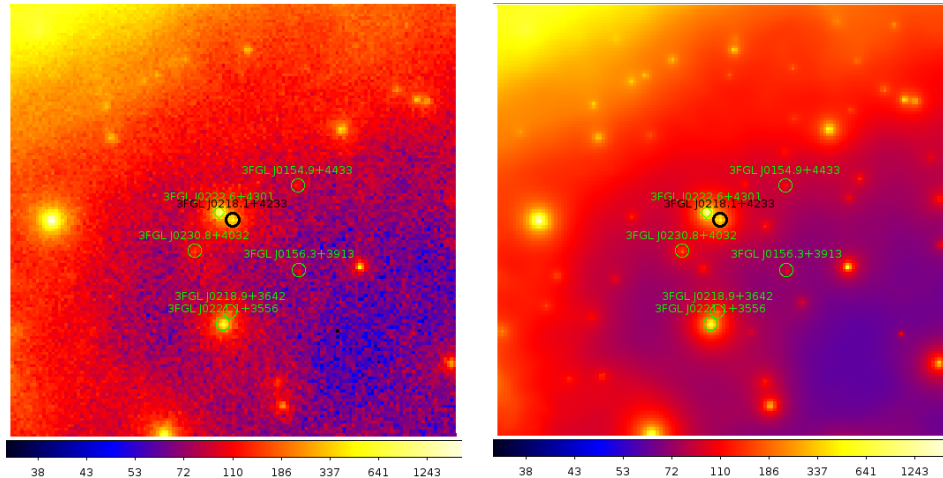


Figure 2.2: The count map of PSR J0218+4232 (left) and the count map generated by the model (right). The target source is in black circle. In the left panel, the green circles represent sources needed to be fitted. The right panel is a count map created according to the fitted spectra model. The size of each figure is 141 pixels \times 141 pixels, and the dimension for each pixel is $0.2^\circ \times 0.2^\circ$.

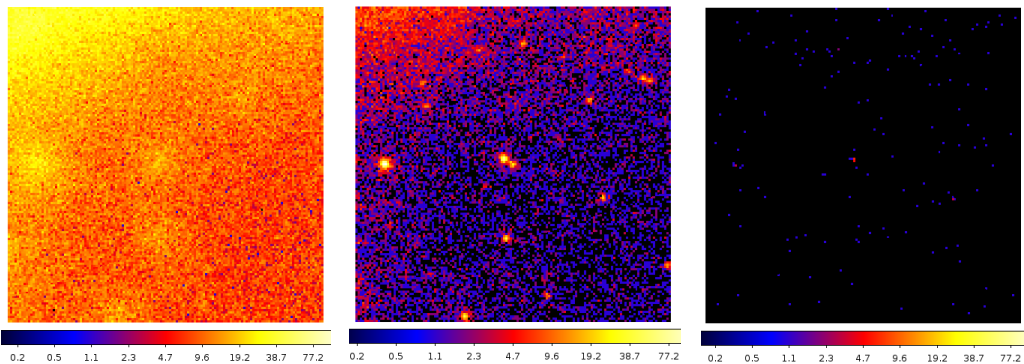


Figure 2.3: Three count maps from PSR J0218+4232's count cube. The energy ranges of the figures are 100~123MeV (left), 1.873~2.310GeV (middle), 35.11~43.29GeV (right).

Figure 2.3 is a comparison between PSR J0218+4232's count maps in different energy bands. The count map of about 100MeV is too noisy to distinguish the target source while the energy is above 30GeV there are so few photons that there is not a clear sign of the source. I choose three circle regions whose centers are the target sources and the radii are 1000 " for all three figures

and then calculate the total numbers of photon counts of the selected regions. As Table 2.3 shows, though the total number of photon counts around the target source is similar between the left and middle count maps, the numbers of counts per energy are much different. Since there are few photons in high energy bands (above 50GeV) compare to other energy bands, I focus more on the lower energy part.

Energy range (MeV)	100~123	1873~2310	35110~43290
Total counts	78	93	0
Counts / MeV (MeV ⁻¹)	3.39	0.21	0.00

Table 2.3: Numbers of photon counts of count maps in different energy bands for PSR J0218+4232.

2.4.2 Binned Likelihood Analysis

Figure 2.2 shows that the fit results of the model are consistent with the observation. However, there are lots of small red pixels in the left panel (generated directly by the observational data) while the right panel is very "clean". This means that a lot of photons are thought as generated by the modeled source. Thus, in the model, the sources are generally slightly brighter than the observation. However, the target source is an exception. In the region I have used before (the center is the target source, and the radius is 1000''), the total photon counts in the left panel are 1815 compare to 1737 in the right panel.

The reason why the count map generated directly by the observational data is a lot more messy is that the source model is generated based on the Fermi database and all sources' spatial positions are fixed. This means that if a photon comes from a particular direction and there is no any known pulsar in that direction, this photon has to be classified into other directions and there

is a modeled source in the direction. Thus, the spatial positions of photons are different between the observation and the model, and the count maps generated directly from models are usually cleaner.

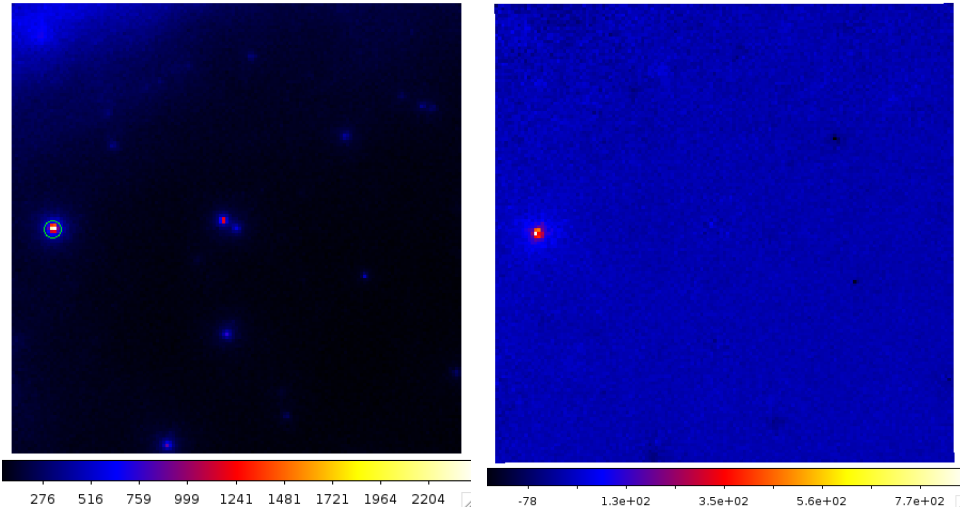


Figure 2.4: The count map and residual map of PSR J0218+4232. The figures are both in linear scale in order to compare the residual map with the original count map more intuitively. The left panel is the count map and the right panel is the residual map which shows the differences between the observation and the spectra model. It is created by directly subtracting the photon counts of each pixel between the count maps of observational data and the spectra model. The green circle region represents (the regions are completely the same in the two figures) the largest number photon counts of the residual map and its radius is $2000''$.

Figure 2.4 basically describes how well the model is compared to the observational data. There are some bright dots in the residual map showing the differences between the spectra model and the observational data. In the residual map of Figure 2.4, most differences of absolute photon counts are small, however, in the green circle region, the absolute value 6003 is large. This means that in this region, the number of photon counts of the observational data (21525) is 6003 larger than in our model. This is not negligible since it is nearly 28% of the original photon counts. Does this mean that the model

is not good? The answer should be yes, however, this does not mean the fit is not good since the model parameters in this region are all fixed and the fixed values are from the *Fermi* LAT four-year Point Source Catalog. Hence, the difference shows some problems of the spectra model, but has nothing to do with the fit results. Instead, from the residual map, we see that the fit results are good because the differences of the number of photon counts are very small, which are about 5% of the photon counts of the count map on average.

Table 2.4 lists the results of the fit parameters. We see from Table 2.4 that the new fit results are consistent with the old ones. However, the precision improves a lot which is ascribed to the *Fermi* LAT four-year Point Source Catalog and PASS 8 dataset. Figure 2.5 is a plot of the spectrum according to Function 2.4. One thing should be noticed is that I need to multiply E^2 to Function 2.4 in order to get the flux. Figure 2.5 shows that the global fit is consistent with flux points fitted by each energy bin separately. The TS value of PSR J0218+4232 is 7110, which gives a significance level $\sigma \approx \sqrt{TS} \approx 84$. This strongly implies the presence of the target source. I also plot TS maps to test the presence of the source as Figure 2.6 shows.

	This Study	Previous Results
Photon Index (Γ)	1.89 ± 0.04	2.0 ± 0.1
Cutoff (E_c , GeV)	3.77 ± 0.40	4.6 ± 1.2
Photon Flux (10^{-8} cm $^{-2}$ s $^{-1}$)	7.29 ± 0.28	7.7 ± 0.7
Energy Flux (10^{-11} erg cm $^{-2}$ s $^{-1}$)	4.45 ± 0.16	4.56 ± 0.24
TS value	6809	1313

Table 2.4: Fit parameters of the spectra model of PSR J0218+4232. The names of parameters are consistent with Equation 2.4. The previous results are reported by Abdo et al. (2013)

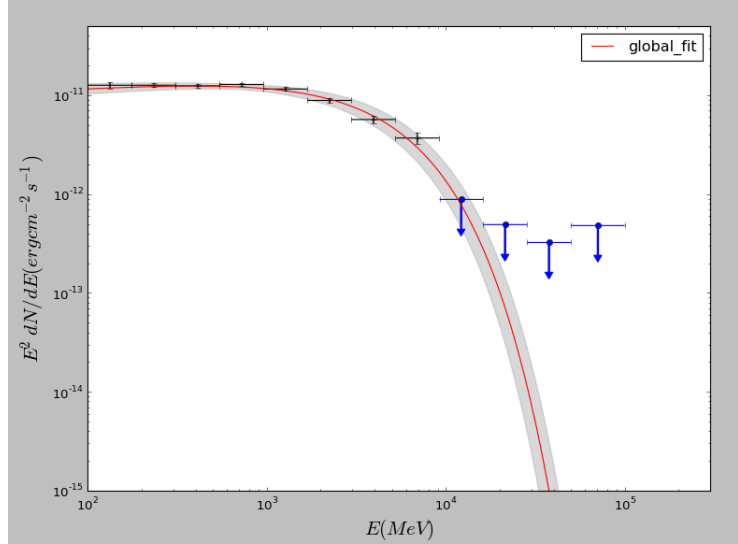


Figure 2.5: The log-log plot of flux to energy of PSR J0218+4232. The grey shade represents fit errors, black points with error bars are flux points, the blue dots are upper values and the red line is the PLEC model multiplied by E^2 . Flux points are fitted separately by dividing the total energy bin ($100 \text{ MeV} \sim 100 \text{ GeV}$) into multiple energy bins. The horizontal error bars represents the width of each bin.

It is also instructive to check the count residuals of the fit as Figure 2.7 shows. The galactic and isotropic emissions are very bright compared with the target source and this can bring some difficulties to the fit (especially for the other two MSPs PSRs B1937+21 and B1821-24). The residuals and fluctuations become larger and more obvious when the energy is larger than 10GeV . At the same time, in low gamma-ray part (from 100MeV to 200MeV), the number of counts of the model deviates from observation counts obviously because of the relatively low energy resolution in the low-energy gamma-ray part. The error of the first bin is larger than the next several bins in Figure 2.5 also shows that the fit in the low-energy gamma-ray band (from 100MeV to 200MeV) is not as good as higher energy bands (but not too high).

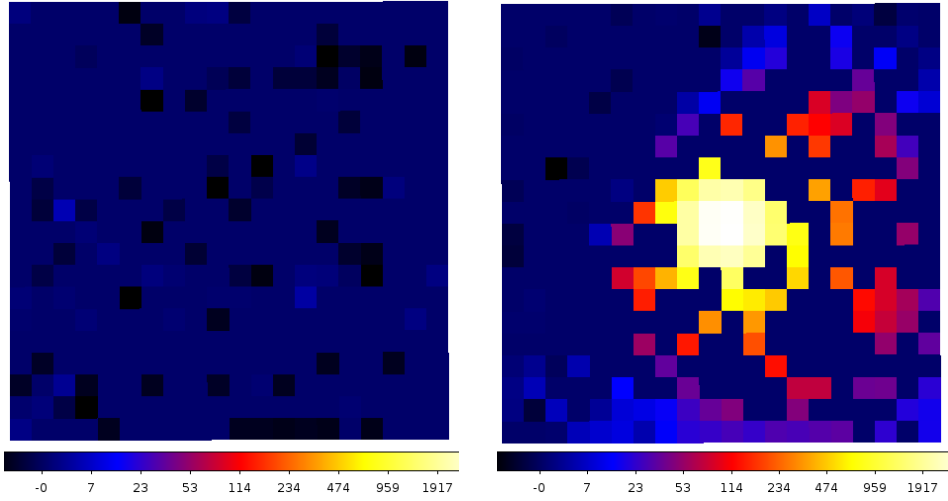


Figure 2.6: TS maps of PSR J0218+4232. The figures' dimensions are $4^\circ \times 4^\circ$ ($20 \text{ pixels} \times 20 \text{ pixels}$ with $0.2^\circ \times 0.2^\circ$ for each pixel). The left and the right panels are generated by the xml models with and without the target source PSR J0218+4232 respectively. The left panel shows that the possibility of adding an imputative point source is very low only with a maximum TS value of less than 5. However, the right panel strongly implies that there should be an additional source after I have removed the target MSP from the spectra model, which means it's highly likely that PSR J0218+4232 is contained in the observation data.

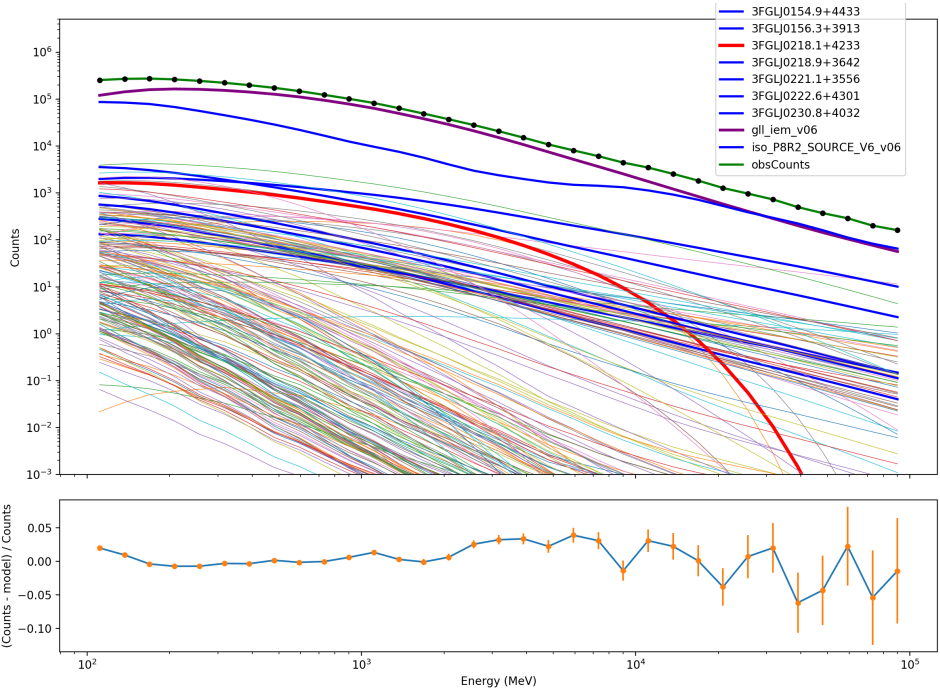


Figure 2.7: The count spectra and count residuals of PSR J0218+4232. The upper panel is the count spectra of all sources included in the fit procedure. Thick lines are those sources with free fit parameters while the thin lines are fixed sources. The green line and the black dots represent observed counts in different energy bands. The purple line represents galactic emissions. The lower panel shows the count residuals in different energy bands.

2.5 PSR B1821-24

The ROI region is also a circle whose radius is 20° and all parameters of sources outside of 8° are fixed. There are six free sources in the region of 8° . Figure 2.8 is a combination of count maps of observational data and the model.

2.5.1 Count Maps And Count Cubes

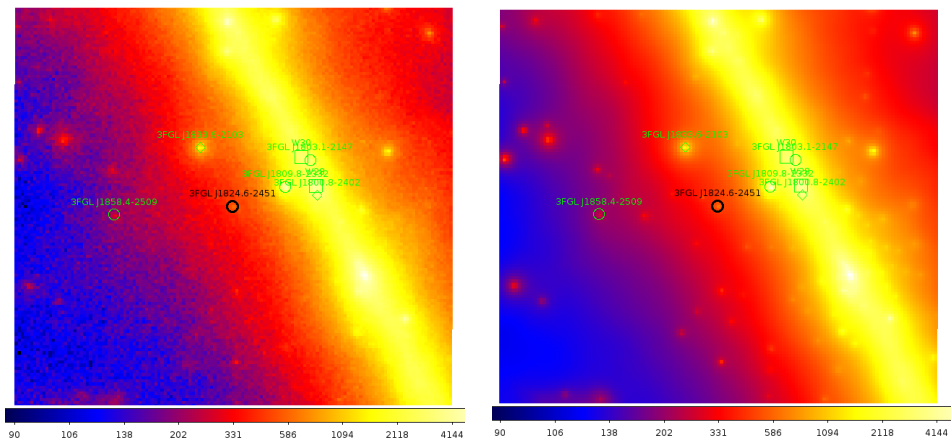


Figure 2.8: The count map of PSR B1821-24 (left) and the count map generated by the model (right). The green circles are sources with free parameters and the black circle is PSR B1821-24. The sizes of the both figures are $141 \text{ pixels} \times 141 \text{ pixels}$, and each pixel's dimension is $0.2^\circ \times 0.2^\circ$.

The left and right panels of Figure 2.10 are the count map of the PSR B1821-24 generated from observational data and spectra model respectively. Like the situations of PSR J0218+4232, the count map from the model is clearly cleaner than from the observational data and the two figures are very similar, which implies that the spectra model describes the observational data well.

Figure 2.9 are count maps of PSR B1821-24 in different energy bands. The target pulsar is too faint in very high energy bands and interfered too much by

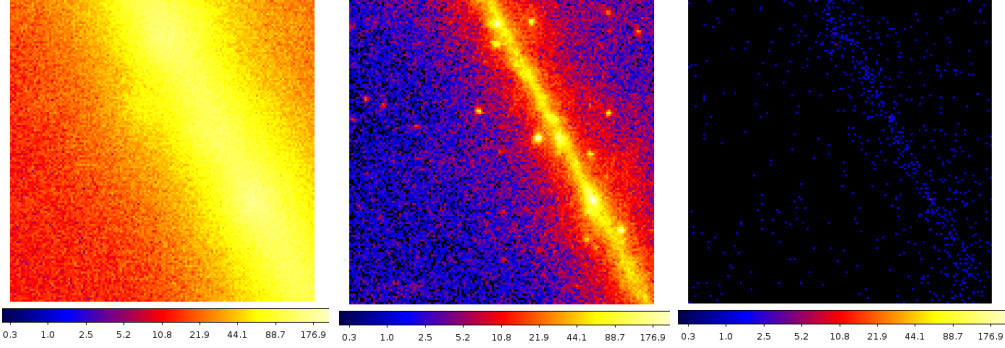


Figure 2.9: Three count maps of PSR B1821-24’s count cube. The energy ranges of the figures are 100~123MeV, 1.873~2.310GeV, 81.11~100GeV respectively from left to right.

the ambient environment in low energy bands (slightly above 100MeV). PSR B1821-24 is in the M28 globular cluster and is the most energetic one, which is much brighter than other sources found in M28. However, since PSR B1821-24 is very faint observed from Earth, it is understandable that the fit results are not as good as the results of PSR J0218+4232.

2.5.2 Binned Likelihood Analysis

The differences of the count map between the observational data and the model are described as Figure 2.10 which is in linear scale. Although there are many red and blue dots in the right panel of the figure, their absolute values are generally small compared with the original counts value. Thus, the fits are acceptable in general. But I am still trying to get the better spectra model.

Table 2.5 shows the global fit results of PSR B1821-24. The TS value of the model is 941 which gives us a significance level of about $\sqrt{941} \sim 31$. This strongly supports the existence of the target source in the observational data. As Table 2.5 shows, the energy flux from 100MeV to 100GeV is not consistent

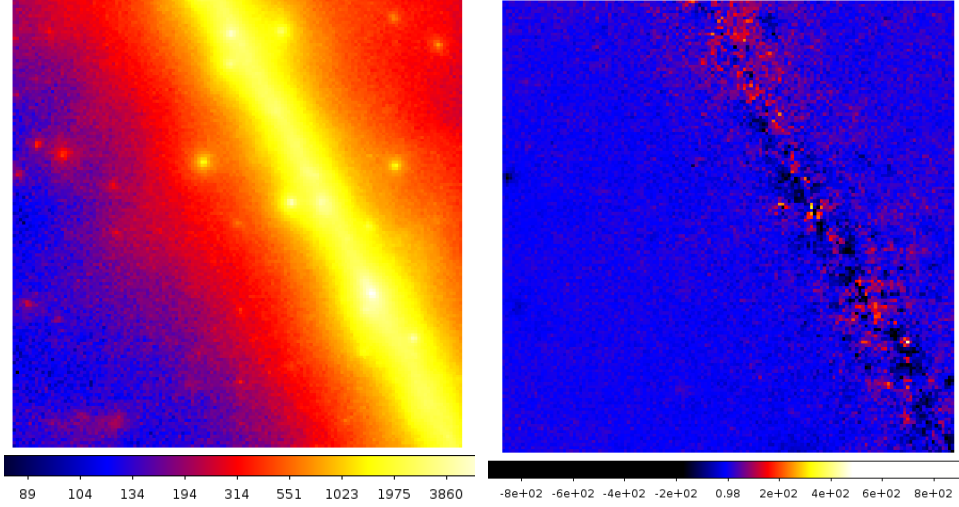


Figure 2.10: The count map and residual map of PSR B1821-24 in linear scale. The left panel is the count map and the right panel is the residual map showing the difference between the observational data and the spectra model.

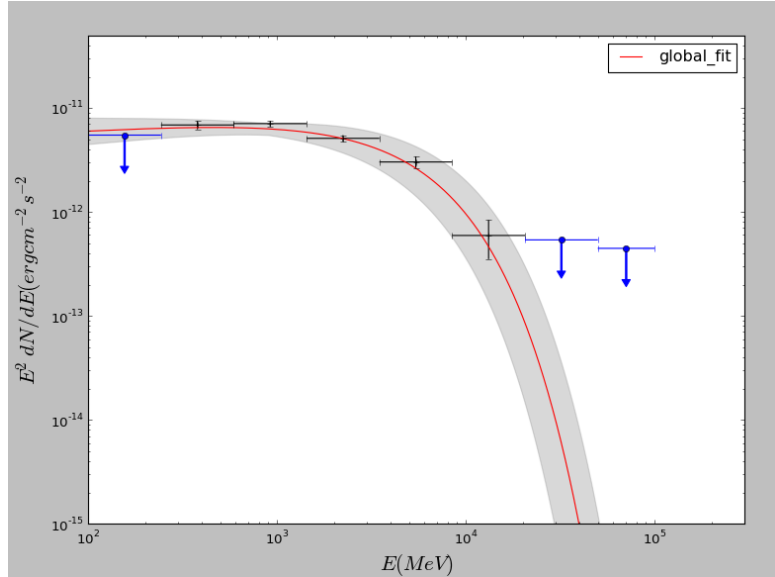


Figure 2.11: The log-log plot of flux to energy of PSR B1821-24's gamma-ray spectrum.

between the two studies and gamma-ray spectrum of the previous study is also softer (Johnson et al. 2013).

Figure 3.3 shows that the global fit is consistent with the flux points generated by fitting sub-energy bins separately. We notice the upper value for the

first energy bin is slightly smaller than the global fit. Though it is strange that the upper value is smaller than the normal value at first glance, it is reasonable since the flux points are fitted separately and are independent to the global fit. In fact, I use a single power-law model to fit each sub-energy bin while PLEC model to do the global fit. As discussed previously, the lower energy parts of the observation (slightly above 100MeV) is not as reliable as other energy bands. As a result, the separate fit for the first energy bin is not as good as the global fit and it is reasonable that the two fit results are not completely consistent. When this happening, I have more confidence in the global fit than the separate fit.

Figure 2.12 contains TS maps of PSR B1821-24. The comparison of TS maps also show the significant of the target MSP. Figure 2.13 shows how well the fit is. Like the count residuals of the other two pulsars, the fit is not good in low energy part (from 100MeV to 500MeV) and high energy band (above 10GeV). Besides, as Figures 2.7, 2.13 and 2.27 show, the numbers of observed photon events are all larger than modeled photon counts for PSRs J0218+4232, B1821-24 and B1937+21.

	This Study	Previous Results
Photon Index (Γ)	1.91 ± 0.07	1.6 ± 0.3
Cutoff Energy(E_c , GeV)	4.50 ± 0.71	3.3 ± 1.5
Photon Flux ($10^{-8} \text{ cm}^{-2}\text{s}^{-1}$)	3.85 ± 0.31	1.5 ± 0.6
Energy Flux ($10^{-11} \text{ erg cm}^{-2} \text{ s}^{-1}$)	2.44 ± 0.14	1.3 ± 0.2
TS value	941	76

Table 2.5: Fit parameters of the spectra model of PSR B1821-24. The names of parameters are also consistent with Equation 2.4.

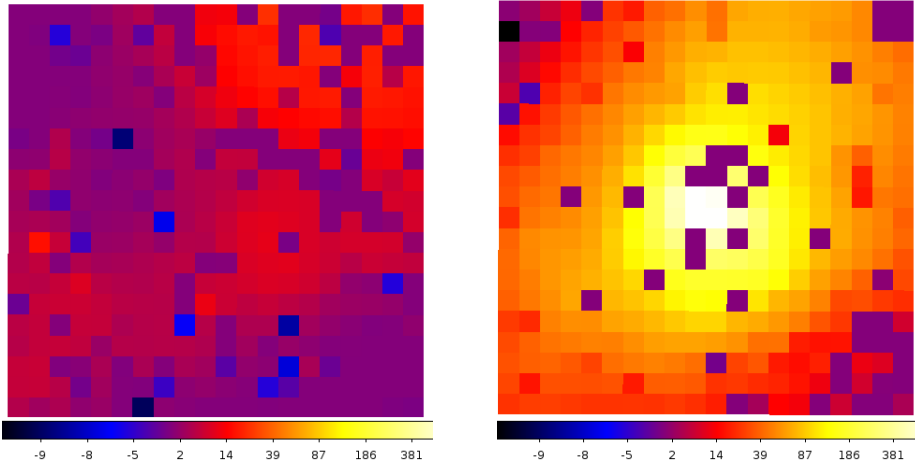


Figure 2.12: TS maps of PSR B1821-24. The figures' dimensions are $4^\circ \times 4^\circ$ (20 pixels \times 20 pixels with $0.2^\circ \times 0.2^\circ$ for each pixel). The left and right panels are generated by the XML models with and without the target source PSR B1821-24 respectively. The left panel shows that the possibility of adding an imputative point source is very low only with a maximum TS value of less than 11 while the TS values of the right figure are generally much larger.

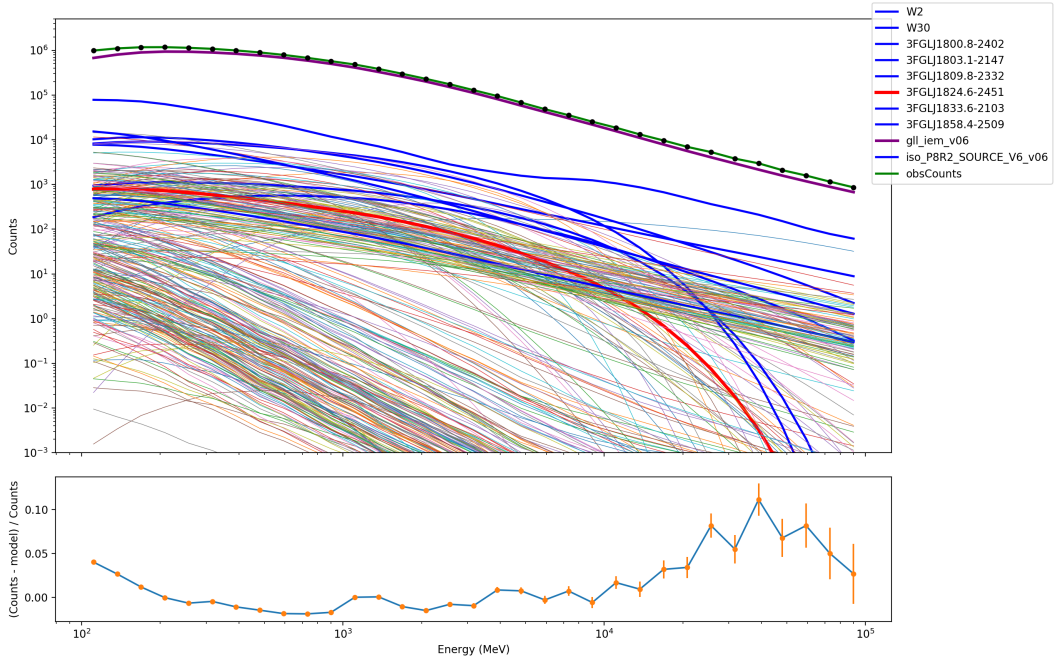


Figure 2.13: The count spectra and count residuals of PSR B1821-24. The upper panel is the count spectra of all sources included in the ROI. Thick lines are those sources with free fit parameters while the thin lines are fixed sources.

2.6 PSR B1937+21

2.6.1 Phase Averaged Analysis

First of all, I use a PLEC model to fit the gamma-ray spectra. In order to make the data analysis be more consistent, I choose the same parameters to process the raw observational data. Like the other two MSPs, the radius of the ROI is 20° degrees, and all parameters of sources 8° degrees outside from the center are fixed with default values. There are nine point sources including the target source PSR B1937+21 and twenty-eight free parameters. In fact, PSR B1937+21 is not included in *Fermi* LAT four-year Point Source Catalog may be because that the MSP is very weak and the signal to noise ratio is so low that the reliable spectrum fit results with a large TS value had not been obtained when the *Fermi* LAT four-year Point Source Catalog was published. Thus I have to add the configuration file for the MSP manually and I set the initial value of photon index to be -2.0 .

Count Maps and Count Cubes

Figure 2.14 is the comparison of count maps between observational data. Like the previous conditions, the count map of observational data is more messy than the fitted model.

Figure 2.15 shows the count maps in different energy bands. When energy is above about 1.6GeV , there are very few photons. In many cases, people analyze spectra from 100MeV to 300GeV with *Fermi* LAT, however, the number of photon counts above 100GeV is nearly negligible compared with the total counts. The total number of photon counts from 100MeV to 300GeV is about

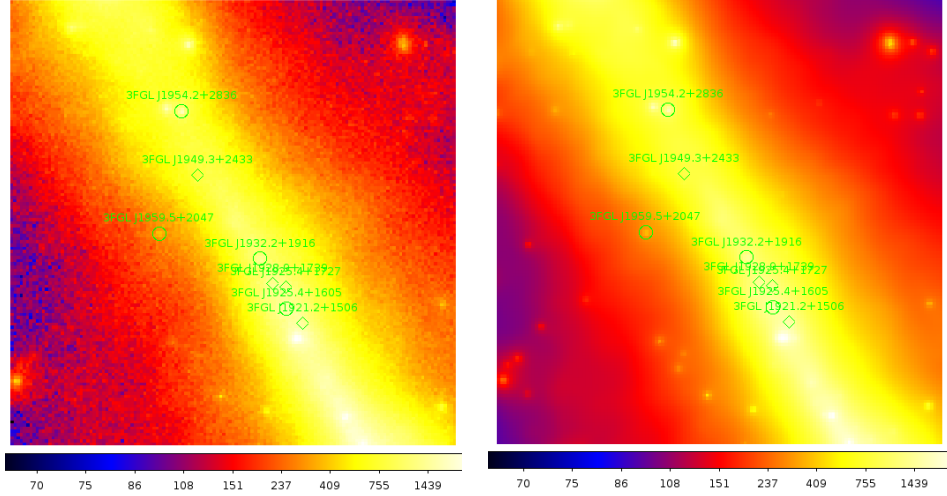


Figure 2.14: The count maps of PSR B1937+21 created from observation data (left) and from the spectra model (right). The dimensions of both figures are 141 pixels \times 141 pixels and each pixel's size is $0.2^\circ \times 0.2^\circ$.

1.07×10^7 compared with 1175 from 100GeV to 300GeV. As a result, it is reasonable to use data only from 100MeV to 100GeV and there should not be any noticeable difference whether I use 100GeV to 100GeV or 100GeV to 300GeV. The case is also true for the other two pulsars — PSRs J0218+4232 and B1821-24.

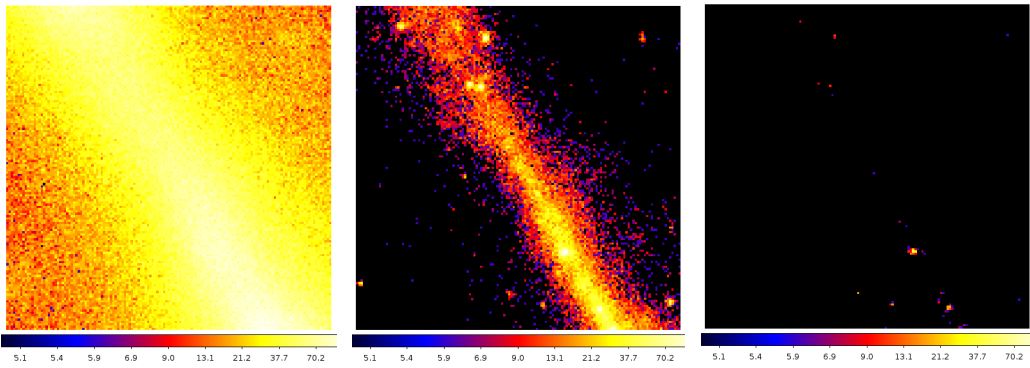


Figure 2.15: Three count maps of PSR B1937+21's count cube. The energy ranges of the figures are from 100 to 131 MeV, from 2460 to 3212 MeV, from 12198 to 15929 MeV respectively.

Binned Likelihood Analysis

Figure 2.16 roughly describes how well the global fit is. Both left and right panel are in linear scale in order to make it easier to compare. As the residual map shows, there is no obvious difference between the fitted model and the observational data. The max value of the photon counts in the residual map is only about 270.

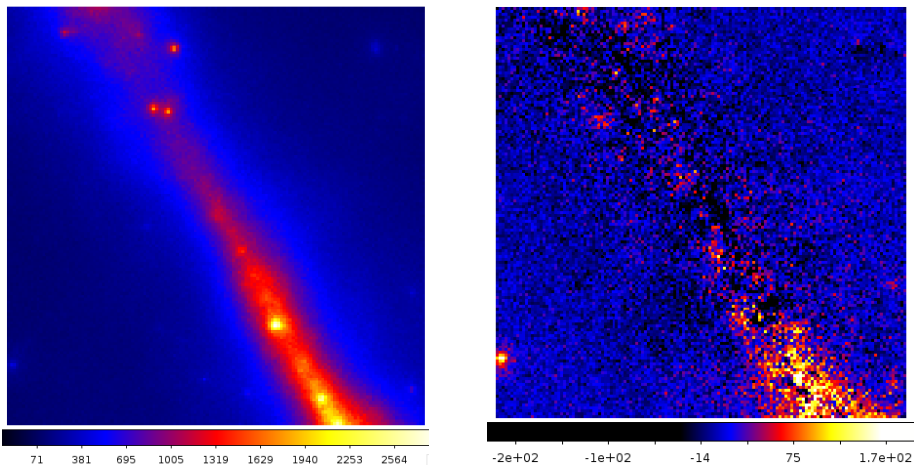


Figure 2.16: The count map created from observational data (left) and residual map (right) of PSR B1937+21. Both left and right panels are in linear scale. The dimension is 141 pixels \times 141 pixels and each pixel's size is $0.2^\circ \times 0.2^\circ$.

Table 2.6 lists the fit results of PLEC model. According to the previous work (Ng et al. 2014)), the PLEC model is not preferred over the power-law model. Therefore, only the results of power-law model are reported in the paper. In this result, the PLEC model gives a TS value of 122, which is about the same as the previous results.

Figure 2.18 shows the residual counts of the global fit. The fit is good from 100MeV to about 20GeV. However, it is significantly worse when the energy is too high and the residual counts are much larger than the PSRs J0218+4232 and B1821-24.

	This Study	Previous Results
Photon Index (Γ)	2.61 ± 0.22	2.1 ± 0.2
Cutoff Energy (E_c , GeV)	4.90 ± 2.29	8 ± 4

Table 2.6: Fit parameters of the spectra model of PSR B1937+21. The names of parameters are consistent with Equation 2.4. The old results are reported by Ng et al. (2014) Note that since the paper prefers power-law model than PLEC model, it does not report the photon flux of PLEC model.

Although the TS value for PSR B1937+21 is only 122, existence in gamma-ray of the target source is more obvious in the TS maps as the Figure 2.17 shows. Figure 2.21 contains the spectra shape of the PLEC model.

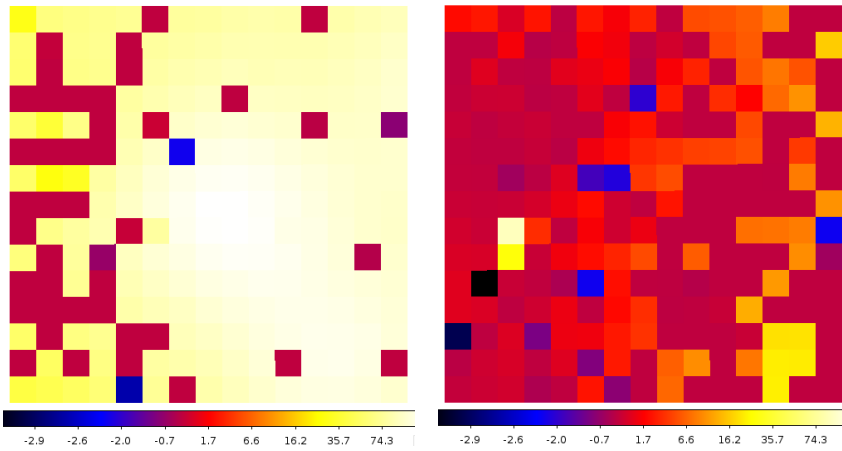


Figure 2.17: TS maps of PSR B1937+21. The dimension is $3^\circ \times 3^\circ$ (15 pixels \times 15 pixels and each pixel is $0.2^\circ \times 0.2^\circ$). The left panel is generated by the model after removing PSR B1937+21 while the right panel contains the target source.

Since the fit results of PLEC model is not very satisfiable, I also fit the gamma-ray spectra with a power-law model. Because I have shown lots of count maps and they actually do not give us very much information, I do not show more count maps and count cubes for the analysis of the power-law model. The photon index is 2.94 ± 0.13 with a TS value of 147 as the Table 2.7 shows. Although the energy flux is consistent with the previous study (Ng et al. 2014), the photon index is not.

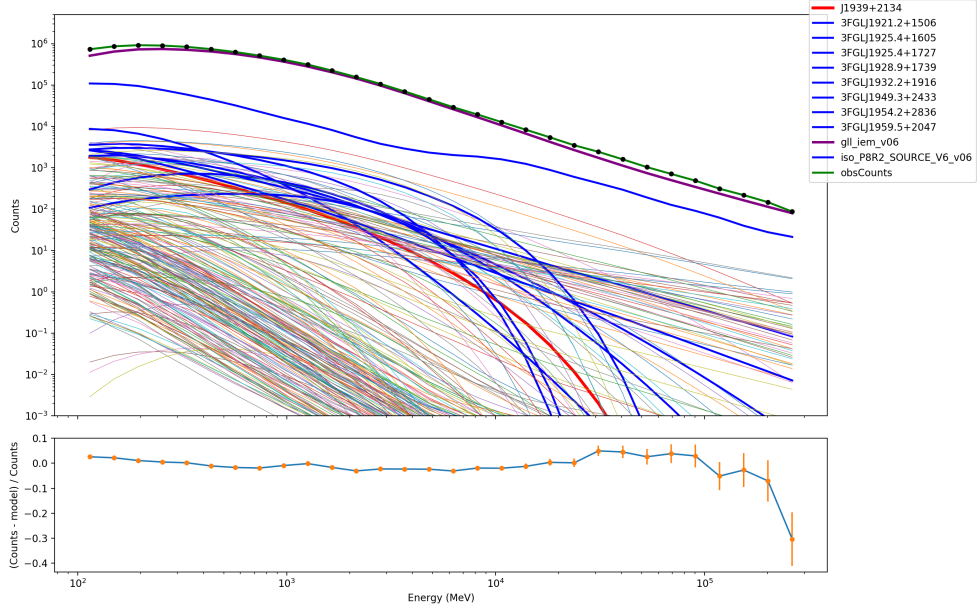


Figure 2.18: Top: count spectra for all sources included in the xml model (including sources with both free parameters and fixed parameters). Bottom: count residuals plot of the model. The thick red line is the target source PSR B1937+21, the blue thick lines are sources with free parameters and the thin lines are the sources with only fixed parameters.

	This Thesis	Previous Results
Photon Index (Γ)	2.94 ± 0.13	2.38 ± 0.07
Energy Flux (10^{-11} erg cm $^{-2}$ s $^{-1}$)	1.6 ± 0.2	1.6 ± 0.2

Table 2.7: Photon index comparison of power-law model between different studies. The data of column Previous Results are from Ng et al. (2014).

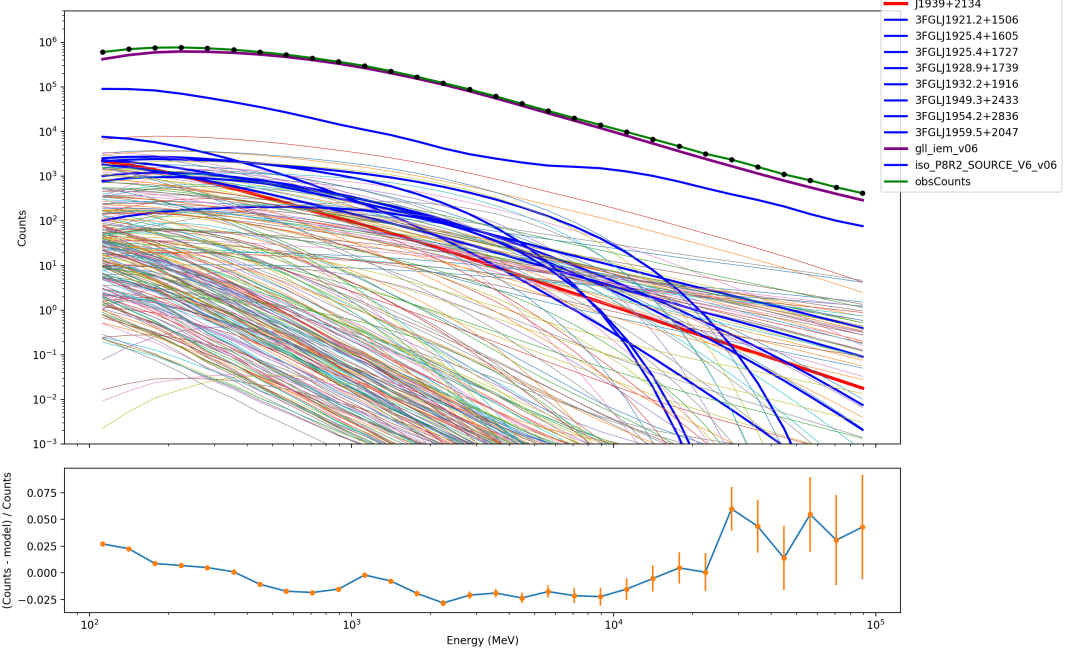


Figure 2.19: Top panel is counts spectra for all sources within the ROI. Bottom panel shows the count residuals.

Figure 2.19 is the count residuals of the fit and it is no better than Figure 2.18. But I also prefer a power-law model since the likelihood of the power-law model is much larger than the PLEC model. The Fermi tool *gtlike* gives a likelihood value of the fitting model. I compare the absolute value of the likelihood to decide which model is preferred. The absolute value for the power-law model is 18409504.4 compared with 4427799.496 for a PLEC model. And the spectrum of the power-law model is shown in Figure 2.21. Both power-law and PLEC models are consistent with the flux points, which are generated independently, and the flux points do not show a clear cutoff.

Figure 2.20 shows the TS maps with the target source and without the target source.

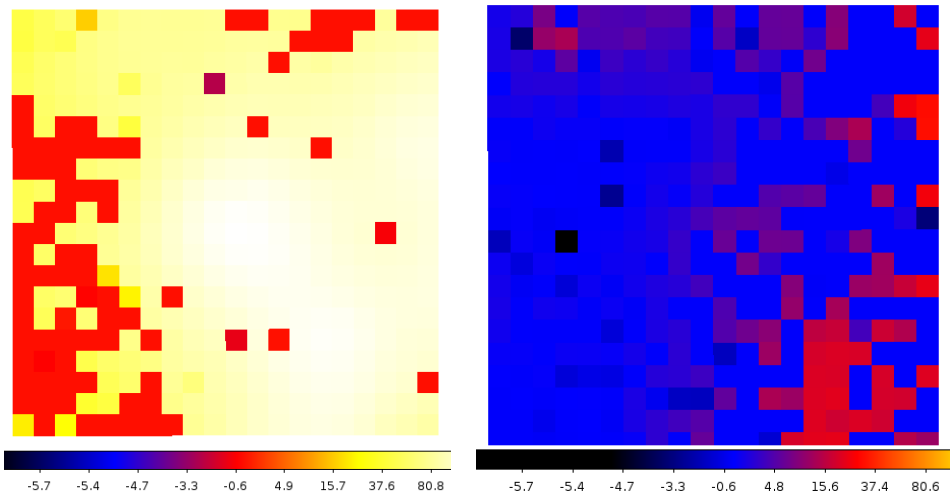


Figure 2.20: TS maps of PSR B1937+21 (power-law model). The dimension is $4^\circ \times 4^\circ$ (20 pixels \times 20 pixels and each pixel is $0.2^\circ \times 0.2^\circ$). The left panel is generated by the model after removing PSR B1937+21 while the right panel contains the target source.

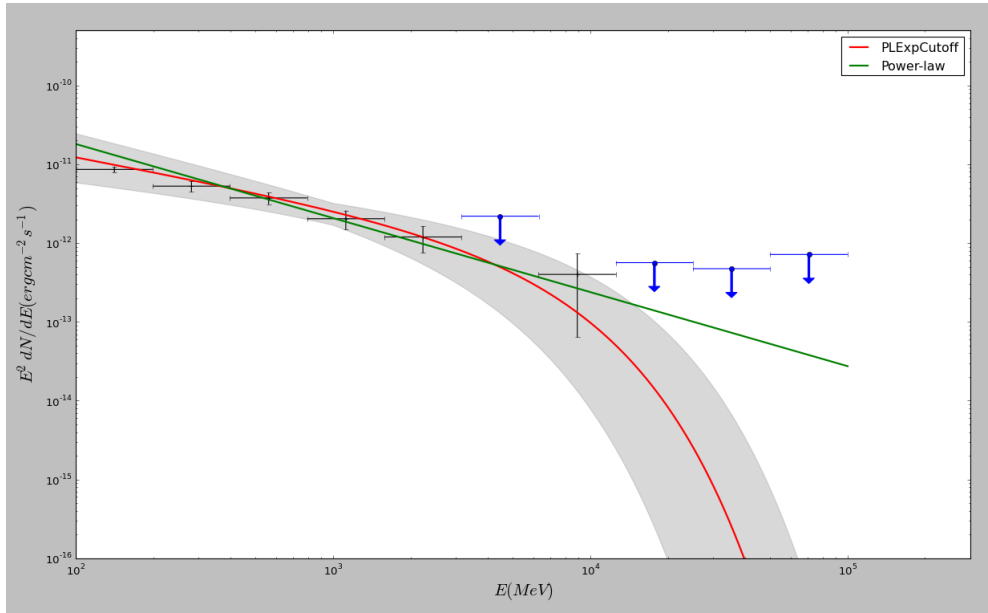


Figure 2.21: The log-log plot of flux to energy of PSR B1937+21's gamma-ray spectrum. The red line represents the PLEC model and the green line is the power-law model.

2.6.2 Phase Resolved Analysis

Since the PLEC model is not a good model for phase-averaged spectrum of PSR B1937+21, I did a quick phase-resolved analysis for the MPS. I choose the phase of $0.0 \sim 0.2$ and $0.5 \sim 0.7$ from the full good time interval (GTI) as Figure 2.22 implies.

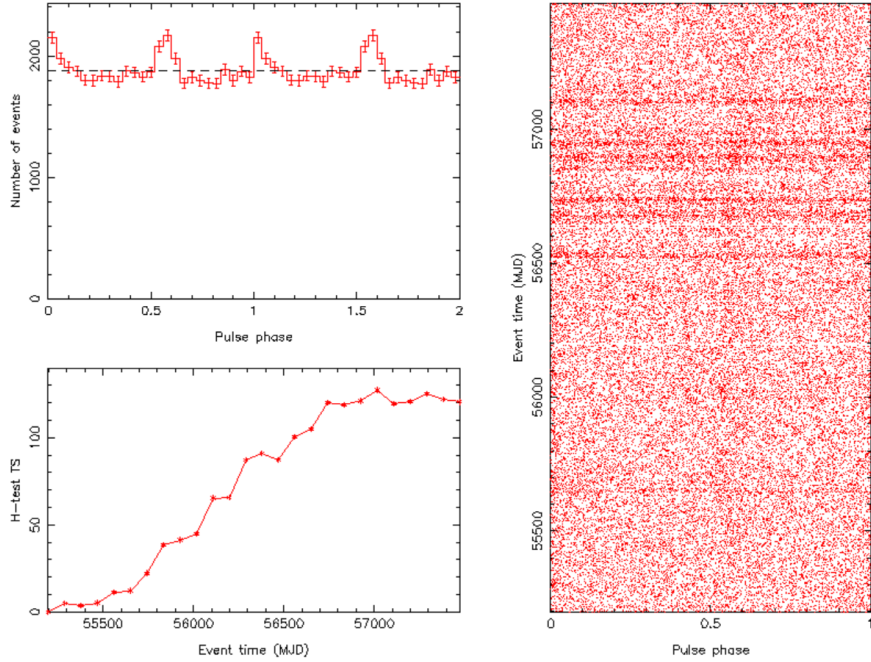


Figure 2.22: Top left panel shows the pulse phase of PSR B1937+21 in gamma-ray band. The figure is produced by tempo2.

The light curve generated by *Fermi* LAT is consistent with previous results (Guillemot et al. 2012) as Figure 2.23 shows. The new light curve by LAT is better than the previous LAT light curve as shown in the figure.

The radius of the ROI is also set to 20° degrees, and all parameters of sources 8° degrees outside from the center are fixed with default values, which is the same as the above analysis. Figure 2.24 is the comparison of count maps between observational data and the model.

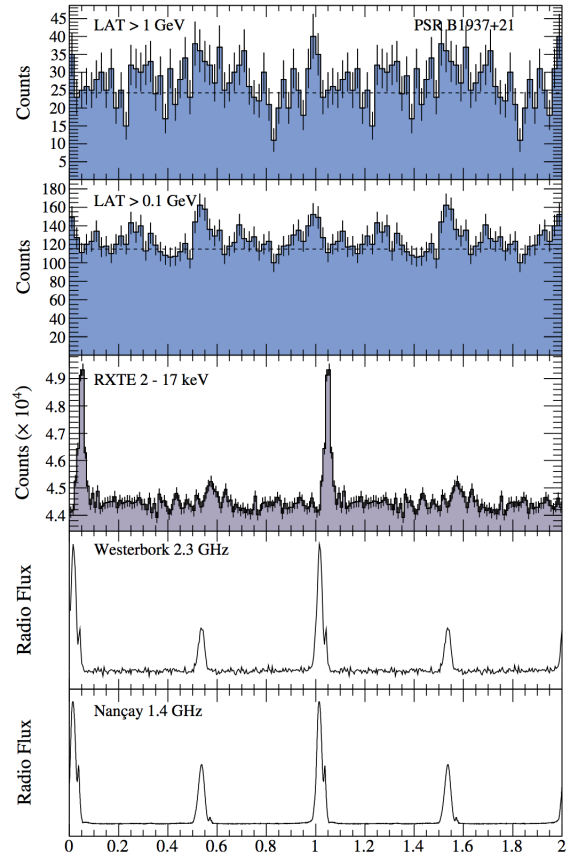


Figure 2.23: Light curves of PSR B1937+21 by different telescopes. The data and figure are from Guillemot et al. (2012)

Count Maps and Count Cubes

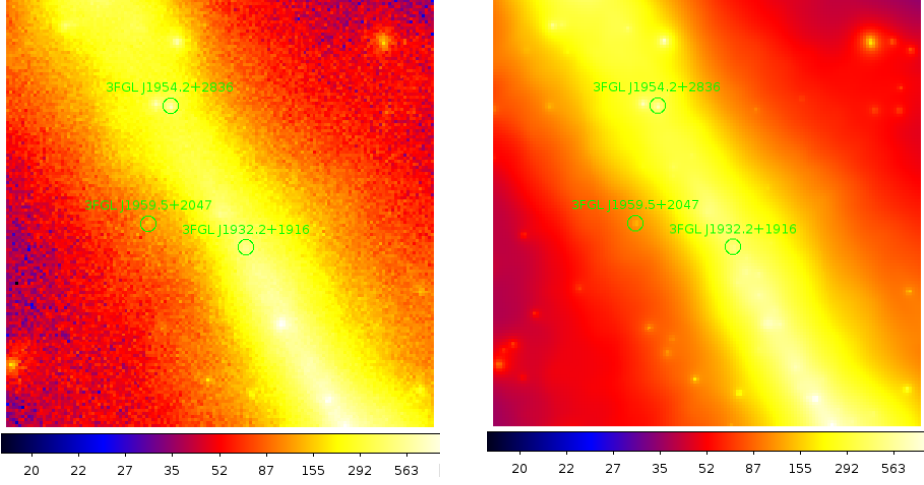


Figure 2.24: The count maps of PSR B1937+21 created from observation data (left) and from the spectra model (right). The dimensions of both figures are 141 pixels \times 141 pixels and each pixel's size is $0.2^\circ \times 0.2^\circ$.

There are four point sources with free parameters in the model which are represented by the green circles in Figure 2.24 and I add the PLEC model for PSR B1937+21 manually.

Like the phase-averaged case, the count map is so messy that the source PSR B1937+21 is completely not identifiable in this count map. Figure 2.25 shows count maps in different energy bands. As the figure shows, the lower energy band is very messy while there is no valuable data in the high energy band. Therefore, the data in the middle energy range is more reliable and when fitting the two-layer model, it has higher priority to minimize the differences between the model and observational data in the middle part.

Binned Likelihood Analysis

Figure 2.26 is a combination of the residual map the original count map of PSR B1937+21 in linear scale. The fact that there are many dots in the

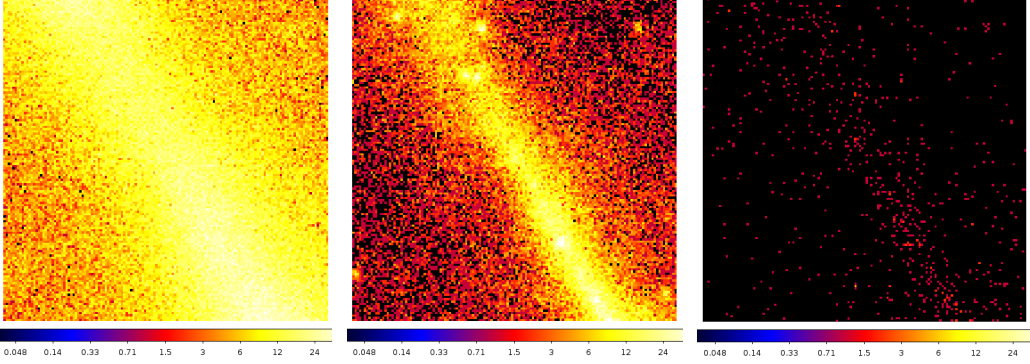


Figure 2.25: Three count maps extracted from PSR B1937+21’s count cube. The energy ranges of the figures are from 100 to 126 MeV, from 1.99 to 2.51 GeV, from 50.12 to 63.10 GeV respectively.

residual map implies that the global fit is not as good as the other two pulsars. Furthermore, the fit is particularly bad in the cyan circle region in the right bottom part Figure 2.26. The total numbers of counts of the cyan region are 18975 and 4212 respectively for the count map and the residual map. The center of the region is $(290.53^\circ, 14.12^\circ)$ and is about 8.65° away from the source, which means that spectral parameters of the sources in the region are fixed during the fit. Therefore, this may be because that the default values from *Fermi* LAT four-year Point Source Catalog (3FGL) in this region are not consistent with the observational data.

The Figure 2.27 is the combination of count spectra for all sources within the 20° and the count residual plot. The count residual plot shows that except low gamma-ray energy part (from 100MeV to 200MeV) and very high energy band (above 10GeV) the total number of photon counts of the model is very close to the observational data. This seems good but also implies some problems. As previously discussed, the modeled number of photon counts in the cyan circle is 7924 smaller than the observational data. And the count residual plot shows that the count number of the whole map is nearly the same, which means that in the model there must be some sources forced to be larger than

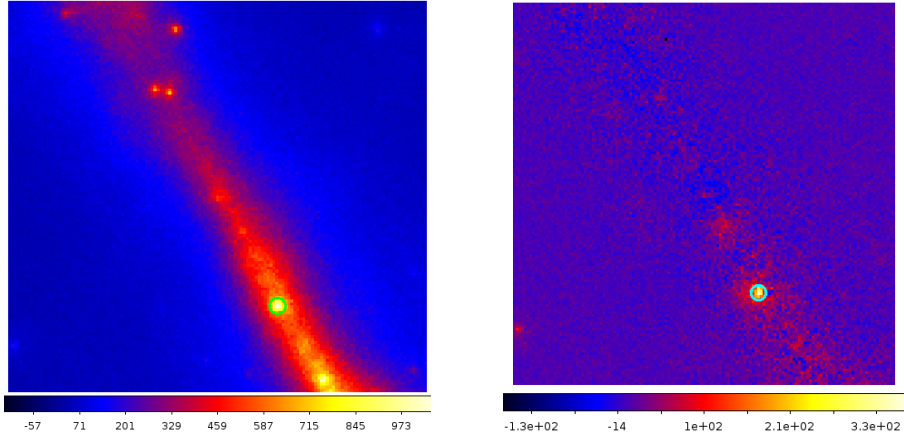


Figure 2.26: The count maps of PSR B1937+21 created from observation data (left) and from the spectra model (right). The dimensions of both figures are 141 pixels \times 141 pixels and each pixel's size is $0.2^\circ \times 0.2^\circ$.

the real value to make up for the deficiency. This implies that the fit results of some sources with free parameters are not as good as the Figure 2.27 shows.

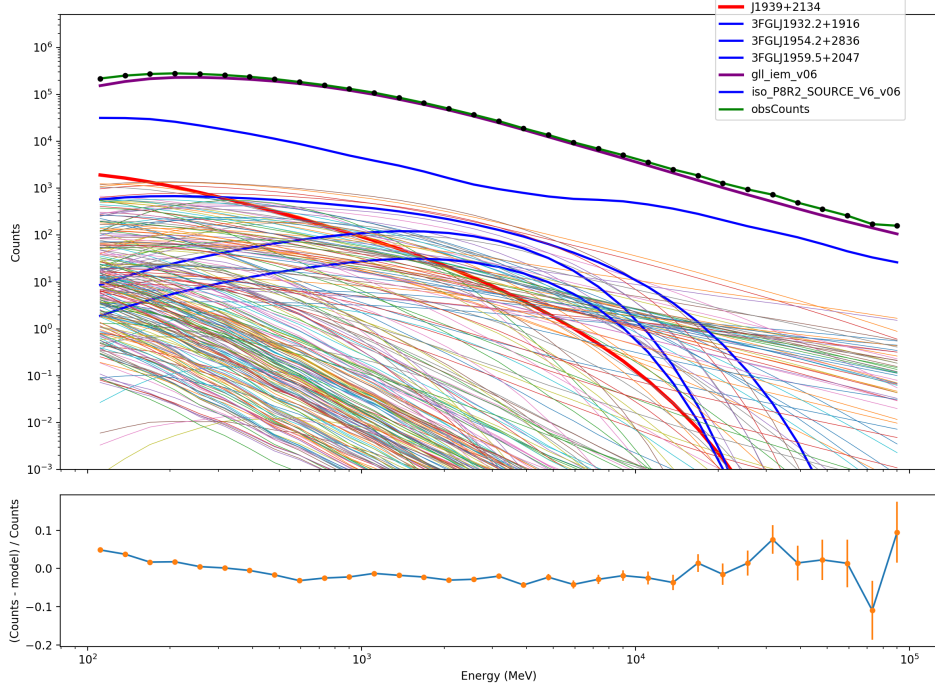


Figure 2.27: The count spectra (top) of all sources including those with only fixed parameters and count residuals (bottom) of the fit for PSR B1937+21.

Table 2.8 lists the results of the fit parameters of PSR B1937+21. We see from the table that the new fit results are consistent with the old ones and

the precision improves a lot. Figure 2.28 is a plot of the PLEC model. The global fit is consistent with flux points fitted by each energy bin separately as the flux points and the red line with shade shows. Surprisingly, the power-law model is very close to the phase-resolved PLEC model. The TS value of our target source is 383, which gives a significance level $\sigma \approx \sqrt{TS} = 19.6$. This implies the presence of the target source. I also generate TS maps to test the presence of the source as Figure 2.29 shows.

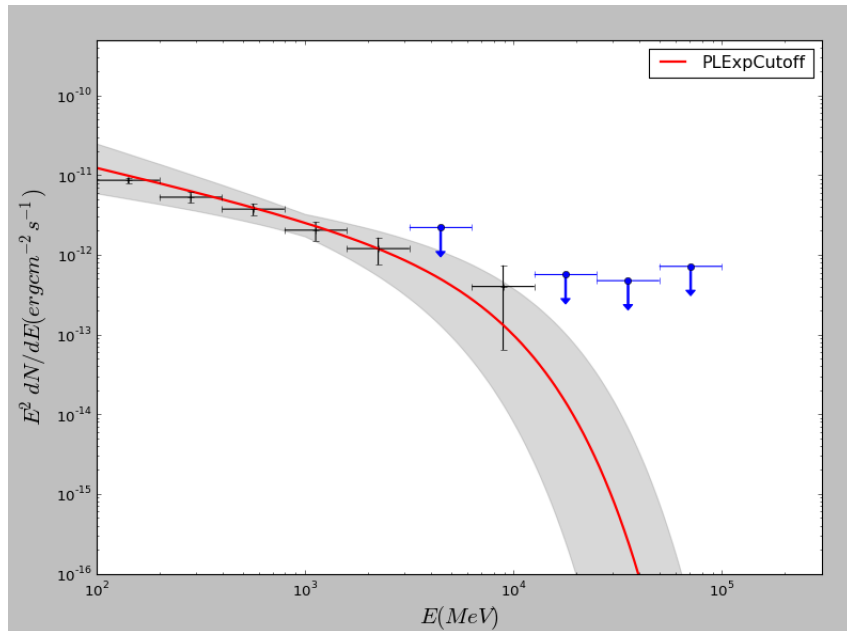


Figure 2.28: PLEC model spectrum of PSR B1937+21 (phase resolved).

	This Study	Previous Results
Photon Index (Γ)	2.37 ± 0.06	1.43 ± 0.87
Cutoff Energy(E_c , GeV)	4.5 ± 1.1	1.15 ± 0.74

Table 2.8: Fit parameters of the spectra model of PSR B1937+21 (phase resolved). The previous results are from Ng et al. (2014). Since the studied energy range is different, I do not list the energy flux for comparison.

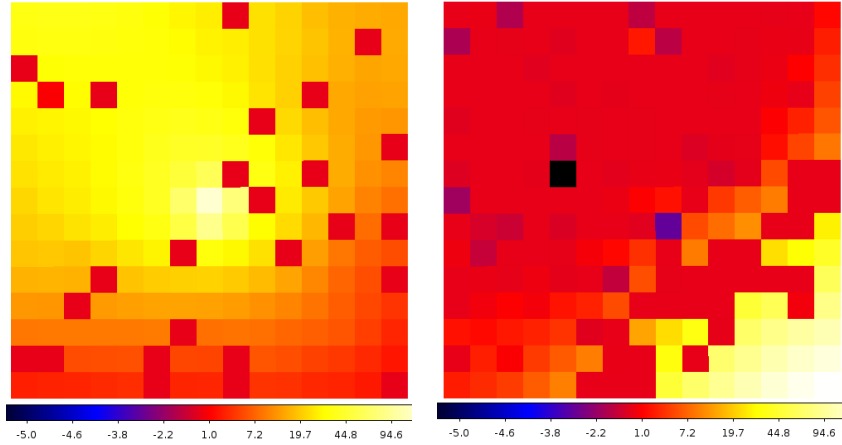


Figure 2.29: TS maps of PSR B1937+21. The dimension is $3^\circ \times 3^\circ$ (15 pixels \times 15 pixels and each pixel is $0.2^\circ \times 0.2^\circ$). The left panel is generated by the model after removing PSR B1937+21 while the right panel contains the target source.

2.7 Summary of the Results

The spectra of PSRs J0218+4232, B1937+21 and B1821-24 are studied using more observation data and newly published *Pass 8* dataset. The new results of the thesis are generally consistent with the old results as the Table 2.9 shows. For PSR B1937+21, I also list the results of power-law model as Table 2.10 shows.

	J0218+2134		B1937+21		B1821-24	
	New	Previous	New	Previous	New	Previous
Photon Index (Γ)	1.89 ± 0.04	2.0 ± 0.1	2.37 ± 0.06	2.1 ± 0.2	1.91 ± 0.07	1.6 ± 0.3
Cutoff Energy (GeV)	3.77 ± 0.40	4.6 ± 1.2	4.5 ± 1.1	8 ± 4	4.50 ± 0.71	3.3 ± 1.5
Photon Flux ($10^{-8} \text{ cm}^{-2}\text{s}^{-1}$)	7.29 ± 0.28	7.7 ± 0.7	3.76 ± 0.35		3.85 ± 0.31	1.5 ± 0.6
Energy Flux ($10^{-11} \text{ erg cm}^{-2}\text{s}^{-1}$)	4.45 ± 0.16	4.56 ± 0.24	1.58 ± 0.15		2.44 ± 0.14	1.3 ± 0.2

Table 2.9: Fit parameters of the spectra model of PSR J0218+4232. The names of parameters are consistent with Equation 2.4. The previous results are from Ng et al. (2014); Abdo et al. (2013)

	New Results	Previous Results
Photon Index (Γ)	2.94 ± 0.13	2.38 ± 0.07
Photon Flux ($10^{-8} \text{ cm}^{-2}\text{s}^{-1}$)	5.89 ± 0.68	2.93
Energy Flux ($10^{-11} \text{ erg cm}^{-2}\text{s}^{-1}$)	1.92 ± 0.18	1.6 ± 0.2
TS value	147	112

Table 2.10: Fit results of power-law model for PSR B1937+21. Since the previous paper does not show the photon flux, I cannot calculate the error bars of photon flux for the previous value.

With *Pass 8* data and more observational data, the new results have smaller error bars in terms of photon index and energy flux. Furthermore, we have much larger TS values for PSRs J0218+4232 and B1821-24 as the Table 2.11 shows.

	J0218+4232	B1821-24	B1937+21
Previous	1313	76	112
New Results	6809	941	147

Table 2.11: TS values comparison between the new results and the previous results for the three MSPs.

Chapter 3

Theory and Simulation

3.1 A Brief Introduction to the Outer Gap Model

It is oversimplified to regard a pulsar as a magnetized sphere rotating in a vacuum. Actually, there are plenty of charged particles in a pulsar's magnetosphere which co-rotate with the pulsar. The creation of charged particles can be described following steps (Sturrock 1971).

In the intense magnetic field, the high energy photons decay into electrons and positrons which are called secondary particles by the process: $\gamma + (B) \rightarrow e^+ + e^- + (B)$ and these charged particles can emit synchrotron radiation. The secondary particles in charge-deficient regions can also be accelerated to very high speed by strong magnetic field just like primary particles and some of them then emit gamma-rays which can further decay into electrons and positrons. As a result, these charged particles can create more secondary particles. This chain of the processes is quite efficient to produce charged particles and make

a pulsar's magnetosphere filled with plasma as a consequence. Therefore, a characteristic charge density $\rho_{GJ} = -\frac{\vec{\Omega} \cdot \vec{B}}{2\pi c}$ called Goldreich-Julian charge density is produced (Goldreich & Julian 1969). By the definition of ρ_{GJ} , there is a surface called null charge surface where ρ_{GJ} is very close or equal to 0.

Since the charged particles cannot move along the magnetic field lines near the light cylinder (they cannot exceed the speed of light), there are closed field lines and open field lines. Charged particles can move out of the magnetosphere along these open field lines. Thus, the charge densities in the regions near the light cylinder can be much smaller than the Goldreich-Julian charge density and electrons and positrons are accelerated to very high speeds by electric fields parallel to the magnetic field lines ($E_{||}$). These regions are called the outer gap which is between the null charge surface and the light cylinder (Cheng et al. 1986).

Since electrons and positrons are accelerated to opposite directions, there are many charged particles moving toward the pulsar's surface. As discussed above, there is no significant electric field to accelerate the incoming particles, they emit softer photons than the photons emitted by the particles moving outward. Furthermore, since the softer photons are close to the stellar surface, they can generate electrons and positrons with the help of high magnetic fields. These charged particles maintain the current moving along the open field lines. Meanwhile, the particles moving from the null charge surface to the light cylinder are largely accelerated by $E_{||}$, and hence emit gamma-rays by curvature radiation. Part of the gamma-rays convert to electron-positron pairs by colliding with soft photons, and the pairs compensate the deficit of charge densities, hence stop the growth of the outer gap. This is the very basic introduction of the outer gap model, which is helpful to understand the two-layer model.

3.2 Two-Layer Model

After reviewing the gamma-ray emission mechanism, we can proceed to the two-layer model on which this thesis is mainly based (Wang et al. 2010). The two-layer model is a variation of the outer-gap model since they both claim that the gamma-ray emission zone is close to the light cylinder. However, in the two-layer model, the outer layer consists of two regions — a primary acceleration region and a screening region.

In the primary region, charged particles moved out of pulsars along the open field lines, so the charge density is usually very low. However, by pair-production processes, a lot of e^- and e^+ are produced. But in the primary region where lots of pairs are created, the charge density doesn't change very much because the pairs have not been separated yet. With the help of the strong electric field, the particles of opposite signs move to opposite directions. As a result, the two-layer model states that above the primary region, a screening region will be created and the charge density is very large because of the accumulation of the charged particles. This is basically the reason why there are two regions in pulsars' outer magnetosphere.

The next issue is that how to describe the distribution of charge densities in these two regions. For simplicity, the model just uses a step function to represent the charge density distribution and a step function can well describe the large charge density difference between the two regions. It uses a magnetic dipole model to approximate the magnetic distribution in the magnetosphere. Since by magnetic dipole model, the magnetic field at one position is only dependent on the position's distance from the source and altitude, the model also ignores the azimuthal distribution of charge density and uses two param-

eters which are distance r and altitude θ to calculate the magnetic field at a particular position.

The two-layer model uses three parameters to express the structure of a pulsar's outer magnetosphere — charge density of the primary region, the total height of the primary region and the screening region and the last one is the ratio of the thickness of the primary region and the screening region. Figure 3.1 shows the basic structure of two-layer model.

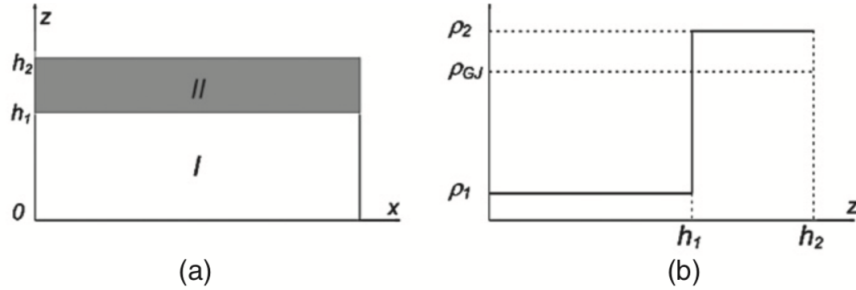


Figure 3.1: (a): Geometry of the two-layer model. h_1 and h_2 is the height of the primary region and the screening region respectively. (b): the charge density distribution of the primary region and the screening region. In the primary region, the charge density is much smaller than Goldreich-Julian charge density while is larger in the screening region. The figure is reported by Wang et al. (2010).

As Figure 3.1 shows, let the charge density of the primary region be $\rho_1 = (1 - g_1)\rho_{GJ}$ and the total gap size be h_2 , where ρ_{GJ} is the Goldreich-Julian charge density. For convenience, also denote the gap size of the primary region as h_1 .

Denote the electrical potential as ϕ_0 which satisfies

$$\nabla^2 \phi_0 = -4\pi\rho_{GJ}, \quad (3.1)$$

and the total electrical potential is $\phi = \phi_0 + \phi'$, where ϕ' is a representation of the deviation from the co-rotating electrical potential. Let the total charge

density be ρ and subtract by Equation 3.1 we have,

$$\nabla^2 \phi' = -4\pi (\rho - \rho_{GJ}). \quad (3.2)$$

Because the model has ignored the distribution in the azimuthal direction, it uses two parameters x, z to represent a position, where x is the direction along the magnetic field line and z is perpendicular to the magnetic field line. In order to solve Equation 3.2, the model also makes two approximations. The first is that the derivative of electrical potential ϕ is ignored. The second is that the Goldreich-Julian charge density is uniformly distributed along the magnetic line direction (x direction). These two approximations are based on a reasonable assumption that the change rate for both electrical potential (ϕ') and Goldreich-Julian charge density (ρ_{GJ}) along the x direction is much smaller than the z direction. As a consequence, Equation 3.2 can be written as:

$$\frac{\partial^2}{\partial z^2} \phi' = -4\pi (\rho - \rho_{GJ}). \quad (3.3)$$

In order to solve Equation 3.3, proper boundary conditions are also needed. First of all, we have to decide the boundary positions, which is determined by four parameters and they can be written as $x_{lo}, x_{hi}, z_{lo}, z_{hi}$. It is reasonable to set x_{lo} and x_{hi} be the stellar surface and the light cylinder respectively and z_{lo} (lower boundary) be the last open field line. And let the electrical potential be 0 along the last open field line (this is because the variation of electric field strength along the x direction is ignored) as Equation 3.4 shows.

$$\phi(x, z_{lo}) = 0. \quad (3.4)$$

To determine the position of z_{hi} is a little bit tricky. In order to make

the electrical potential be continuous at $z = z_{hi} = h_2$, the model sets the $\phi'(z = h_2) = 0$ since the non-co-rotating electrical potential outside the upper bound is 0 and the co-rotating potential is continuous near the boundary. Additionally, because $\phi'(z = h_2-) = 0$ and $\phi'(z = h_2+) = 0$, it is known that the first derivative $\partial\phi'/\partial z|_{z=h_2}$ is 0, which means $E_\perp|_{z=h_2} = 0$. In order to solve Equation 3.3, denote charge densities of the two regions for convenience as the function 3.5 shows.

$$\rho(z) = \begin{cases} \rho_1, & \text{if } (0 \leq z < h_1) \\ \rho_2, & \text{if } (h_1 \leq z \leq h_2). \end{cases} \quad (3.5)$$

With definition in Equation 3.5 and the three boundary conditions, the solution of Equation 3.3 is,

$$\phi'(z, x) = -2\pi \begin{cases} (\rho_1 - \rho_{GJ}(x)) z^2 + C_1 z, & (0 \leq z < h_1) \\ (\rho_2 - \rho_{GJ}(x)) (z^2 - h_2^2) + D_1 (z - h_2), & (h_1 \leq z \leq h_2), \end{cases} \quad (3.6)$$

where

$$C_1 = \frac{(\rho_1 - \rho_{GJ}(x)) h_1 (h_1 - 2h_2) - (\rho_2 - \rho_{GJ}(x)) (h_1 - h_2)^2}{h_2},$$

and

$$D_2 = \frac{(\rho_1 - \rho_2) h_1^2 - [\rho_2 - \rho_{GJ}(x)] h_2^2}{h_2}.$$

From Equation 3.6 and apply $\rho_{GJ}(x) = -(\Omega B x) / (2\pi c s)$ we can directly derive the strength of electrical fields parallel to magnetic field lines as a function of z as Equation 3.7 shows.

$$E'_\parallel(z) = \frac{\Omega B}{c s} \begin{cases} -g_1 z^2 + C'_1 z, & (0 \leq z < h_1) \\ g_2 (z^2 - h_2^2) + D'_1 (z - h_2) & (h_1 \leq z \leq h_2). \end{cases} \quad (3.7)$$

where

$$C'_1 = \frac{g_1 h_1 (h_1 - 2h_2) + g_2 (h_1 - h_2)^2}{h_2},$$

and

$$D'_2 = -\frac{(g_1 + g_2) h_2^2 + g_2 h_2^2}{h_2}.$$

Since charged particles are accelerated in the primary region to relativistic speeds and then emit curvature radiation, we have

$$eE'_{\parallel}c = l_{cur}, \quad (3.8)$$

where E'_{\parallel} is the electric field strength along the magnetic field line described in Equation 3.7. Lorentz factors of the charged particles is estimated according to Equation 3.9.

$$l_{cur} = \frac{2e^2 c \gamma_e^4}{3s^2}, \quad (3.9)$$

where s is the radius of curvature. Combining Equations 3.8 and 3.9 we get expression for Lorentz factor:

$$\gamma_e = \left(\frac{3s^2}{2e} E'_{\parallel} \right)^{1/4}. \quad (3.10)$$

With the Lorentz factor of a charge particle known, we can derive the curvature radiation spectrum for a single charged particle and then can get the total spectrum by integrating over all charged particles. This is the simplified idea of the two-layer model.

3.3 X-ray Emission Model

The three MSPs have very hard photon indices which is about one as Table 3.1 shows. The hard photon indices can be explained by inverse-Compton scattering between the radio waves and the primary particles in the outer magnetosphere. The hard X-ray flux is contributed by both inverse-Compton scattering and synchrotron radiation emitted by the secondary particles.

Firstly, we consider inverse-Compton scattering. Ng et al. (2014) uses a broken power-law model with a turnover at 10MHz to describe the radio spectrum as Function 3.11 shows (Ng et al. 2014).

$$F_{rad}(\nu) = A \begin{cases} \left(\frac{\nu}{100\text{MHz}}\right)^{\beta_1} & \text{for } \nu \geq 10\text{MHz} \\ \left(\frac{10\text{MHz}}{100\text{MHz}}\right)^{\beta_1} \left(\frac{\nu}{10\text{MHz}}\right)^{\beta_2} & \text{for } \nu > 10\text{MHz}. \end{cases} \quad (3.11)$$

The spectral index β_2 is fixed to be 0.5 and β_1 is estimated by the flux densities at 1.4GHz (F_{1400}) and 400MHz (F_{400}). The data used in the thesis are listed in Table 3.2.

By approximating the magnetic field lines as concentric circles, the collision angle between radio waves and primary particles can be estimated by $\sin \theta_0 \sim \sqrt{2f}$, where f is the fractional gap size which is the ratio of the total gap size to the length of the light cylinder. According to Ng et al. (2014), inverse-Compton radiation power per unit energy per solid angle can be estimated by Function 3.12,

$$\frac{dP_{IC}}{d\Omega} = \mathcal{D}^2 (1 - \beta \cos \theta_0) F_{rad} \frac{d\sigma'}{d\Omega'}, \quad (3.12)$$

where θ_1 is the angle between the scattered photon and the primary particle, F_{rad} is the radio spectrum as discussed above, $d\sigma'/d\Omega'$ is the Klein-Nishina

cross section in electron-rest frame, $\mathcal{D} = \gamma^{-1}(1 - \beta)$. Therefore, with the Functions 3.12 and 3.11, the flux of inverse-Compton radiation can be calculated.

Secondly, secondary particles can also emit non-thermal hard X-rays. Although it may not be as strong as inverse-Compton scattering in very hard X-ray band, it should also be included. As previously introduced, some particles are accelerated by the electric fields parallel to the magnetic field lines (E_{\parallel}) and move toward the stellar surface. These particles can heat up the polar cap region to about 1MK (Takata et al. 2012). Then new electron-positron pairs can be created by collisions between the thermal X-rays and gamma-rays. The optical depth can be calculated by Function 3.13,

$$\tau_{X_{\gamma}} = \frac{L_t \sigma_{X_{\gamma}} R_{lc}}{4\pi R_{lc}^2 c k_B T}, \quad (3.13)$$

where T is the surface temperature and L_t is the thermal radiation, $\sigma_{X_{\gamma}} \sim \sigma_T/3$ and k_B is the Boltzmann constant. Then the distribution of the secondary pairs can be described by Function 3.14,

$$\frac{dN}{d\gamma_s}(\gamma_s) = \frac{m_e c^2}{\dot{E}_{sync}} \int_{2\gamma_s m_e c^2}^{\infty} Q(E'_{\gamma}) dE'_{\gamma}, \quad (3.14)$$

where γ_s is the Lorentz factor of the secondary particles, \dot{E}_{sync} is the energy loss rate of the synchrotron radiation. According to Ng et al. (2014), the synchrotron spectrum can be calculated by Function 3.15,

$$F_{sync}(E_{\gamma}) = \frac{\sqrt{3}e^3 B \sin \theta_s}{h m_e c^2} \int \frac{dN}{d\gamma_s} F\left(\frac{E_{\gamma}}{E_{sync}}\right) d\gamma_s, \quad (3.15)$$

where $E_{sync} = 3he\gamma_s^2 B \sin \theta_s / 4\pi m_e c$ and $\sin \theta_s \sim \sqrt{2f}$, which is like the approximation in the inverse-Compton scattering model.

Add the synchrotron radiation and inverse-Compton scattering together, we can calculate the flux in hard X-ray and gamma-ray bands. In addition, by adding the observational data from *NuSTAR* (Gotthelf & Bogdanov 2017), we generate broadband spectra for all the three MSPs.

	J0218+4232	B1937+21	B1821-24
Photon Index (Γ_X)	1.10 ± 0.06	0.9 ± 0.1	1.23 ± 0.03
Luminosity ($L_X, 10^{32} \text{ erg s}^{-1}$)	3.3	6.8	14
Pulse Fraction (%)	64 ± 6	~ 100	82.5 ± 4

Table 3.1: X-ray Properties of the PSRs J0218+4232, B1937 and B1821-24. The data are from Bogdanov et al. (2011); Webb et al. (2004); Kuiper et al. (2002); Huang et al. (2012); Becker et al. (2010)

	J0218+4232	B1937+21	B1821-24
$F_{400} \text{ (mJy)}$	35 ± 5	40	240
$F_{1400} \text{ (mJy)}$	0.9 ± 0.2	2.0 ± 0.4	13.2 ± 5

Table 3.2: Flux densities of PSRs J0218+4232, B1937+21 and B1821-24. The data are from the ATNF catalogue.¹

3.4 Simple Optimizations of Numerical Calculation

3.4.1 Accuracy

To make sure the numerical computation be right is the most important. The first consideration is underflow and overflow of floating digits. One possible condition is calculating speeds of relativistic charged particles with Lorentz factor γ . By doing some simple test, I find that for $\gamma < 1.5 \times 10^7$, the results

are precise enough. However, there are significant rounding errors when $\gamma > 5 \times 10^7$, which means that the results might be wrong for highly energetic particles if I directly use the formula $\beta = \sqrt{1 - 1/\gamma^2}$. Likely, in the two-layer model, nearly all particles have $\gamma < 1 \times 10^7$. Furthermore, there are nearly no situations where double precision floating digits cannot handle calculation results of the two-layer model. Thus, as long as using 64-bit floating digits instead of 32-bit floating digits, we are free from overflowing and underflow errors.

There are some cases when a whole function can be calculated while some parts of them are not. Take Function $f(x) = x \times 1/x$ for example. When x is too large, it can not be expressed by a computer and multiplication is not associative when doing floating point operation. I encounter some situations like this. The formula of curvature radiation spectrum contains modified Bessel function of order $5/3$. In order to speed up the program, I use a polynomial to express the Bessel function, as Equation 3.16 shows.

$$K_{5/3}(x) \simeq a \left(\frac{1}{x} + b \right)^{-cx-1/3} \sqrt{\frac{\pi}{2}} e^{-x-d} \sqrt{x+d} \left[1 + \frac{55}{72(x+d)} - \frac{10151}{10368} (x+d)^2 \right], \quad (3.16)$$

where a, b, c, d are just positive constants and $c = 0.96 < 1$. As a result, the part $(1/x + b)^{-cx-1/3}$ in Function 3.16 is infinity when x is large though the total function is approximated to 0. Thus, I have to explicitly assign the result to be 0 instead of calculating it. Indeed, this error is not easy to find since in most cases the results are not infinity.

3.4.2 Speed of Computation

I did not check any accurate benchmarks in the following discussions and they depend on the average time of the simulations. The most obvious solution is

to use multicores to do the computation. However, most library functions do not support run concurrently and only run on a single core. For example, I need to do many integrations and the speed of integration is critical. I write some simple functions to utilize four CPU cores at the same time when doing integration. This gives me a huge performance improvement.

Furthermore, there are some facts about the basic operations. For instance, add is faster than multiplication which is faster than division. Multiplications and divisions are not associative between floating points. Though the performance differences between different operations for integers can usually be optimized away by modern compilers, the compilers can do nothing for floating points. Thus, I have to do it by ourselves. For example, I have $z^2 - h_2(x)^2$ in function 3.7. In this formula, there are multiplications and one subtraction. After re-writing it to $(z - h_2)(z + h_2)$, we have one addition, one subtraction and one multiplication. Since addition and subtraction is not slower than multiplication, it has no performance harm by the rewriting. What need to be noticed is that the multiplication may not be slower than addition and it is dependent on machines. However, a division is definitely slower than the other three operations. Therefore, in our program, expressions like $1/3$ are rewritten to $1 * 0.3333$ and so on.

Finally, since the program is written in C++, I use some new features of C++ to speed up the calculation. For instance, the keywords ‘constexpr’ and ‘auto’ is used a lot. Meanwhile, I am really careful when allocate arrays trying to make the array fit into cache.

3.5 Numerical Calculation of Spectra Based on the Two-Layer Model

After understanding the theory part of the two-layer model, I then carried out numerical calculations of the spectra for the three MSPs based on the theory.

There are three independent parameters in the calculation. The first parameter is fractional gap size $f = h_2/R_{lc}$, where h_2 is the total gap size including both the primary acceleration region and the screening region and R_{lc} is the radius of the light cylinder. The second parameter is g_1 so that the charge density in the primary accelerating region is $(1 - g_1) \rho_{GJ}$, where ρ_{GJ} is the Goldreich-Julian charge density. The third parameter is the ratio between the sizes of the two gaps (h_1/h_2). Note that I only need to set the charge densities in the primary acceleration region as an independent parameter, since the charge densities in the two gaps are related to each other. Figures 3.2, 3.3, and 3.4 are the spectra of the three MSPs generated from the two-layer model and the results of the fit parameters are listed in Table 3.3. Other than the low energy and high energy gamma-ray bands, the model is consistent with the observation data in terms of the gamma-ray part.

Pulsar Name	f	g_1	h_1/h_2
J0218+4232	0.330	0.920	0.915
B1821-24	0.247	0.955	0.920
B1937+21	0.320	0.975	0.925

Table 3.3: The results of fit parameters for the three MSPs. The physical meaning of each parameter is consistent with the two-layer model described above.

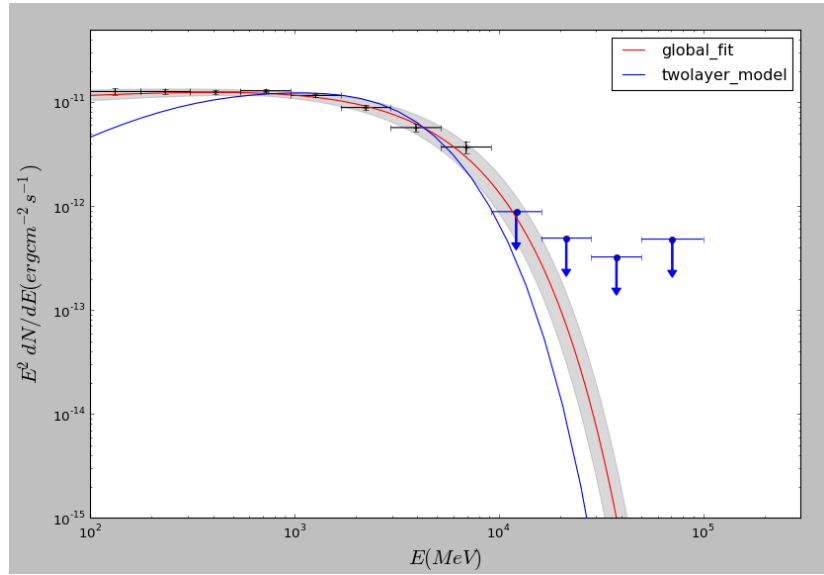


Figure 3.2: The observed gamma-ray spectrum of PSR J0218+4232 compared with the two-layer model.

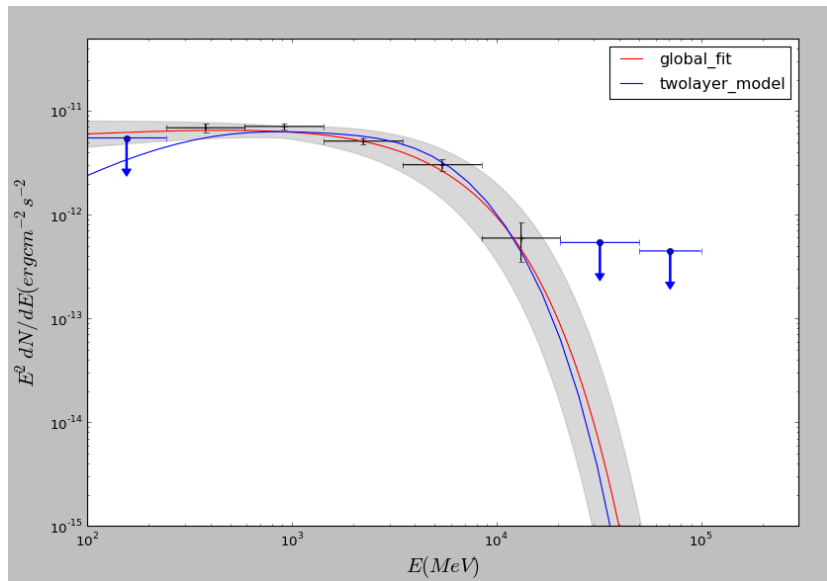


Figure 3.3: The gamma-ray spectrum of PSR B1821-24 by the two-layer model.

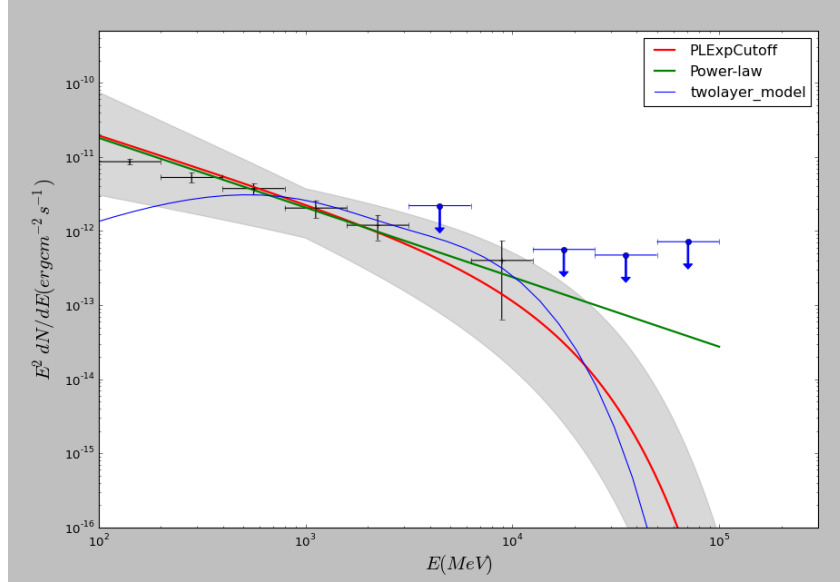


Figure 3.4: The gamma-ray spectrum of PSR B1937+21 by the two-layer model. (blue line)

After obtaining the spectral fit results in the gamma-ray band, I then generated broadband spectra as Figures 3.5, 3.6, and 3.7 show. The hard X-ray data are from Gotthelf & Bogdanov (2017). By tweaking the independent parameters of the two-layer model, I can make the modeled spectra very close to the observational data in the hard X-ray bands. Since the lack of data in the energy band from about 100keV to 100MeV, it is hard to tell if the two-layer model describes the right physical scenario in this energy range. However, the prediction made by the simplified two-layer model is generally accurate. In addition, the model is very intuitive, which is also a very important consideration for building a model. Just as the famous words "With four parameters I can fit an elephant, and with five I can make him wiggle his trunk" said by John von Neumann, in principle, we can fit any data by adding independent parameters. Therefore, in order to test if a theoretical model is good or not, not only we need to consider how precisely the model can predict, but also the physical meaning behind the model. In this sense, the two-layer model is a good start of explaining emission mechanism of pulsars.

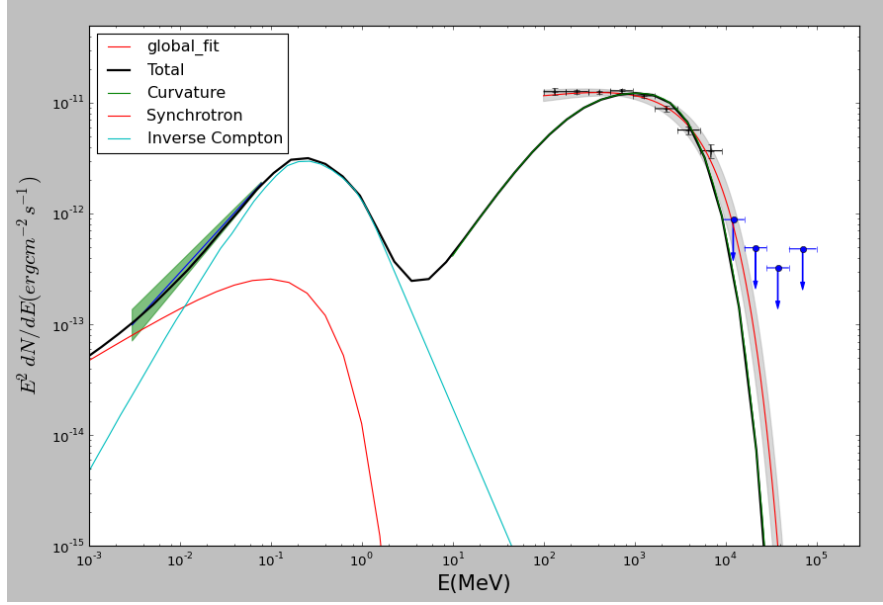


Figure 3.5: The broadband spectrum of PSR J0218+4232. The grey shade is the error of the global fit. And the green shade in the left panel of the figure represents the error of hard X-ray spectrum. The ‘Total’ legend represents the total flux combining the synchrotron radiation, inverse-Compton radiation and curvature radiation altogether.

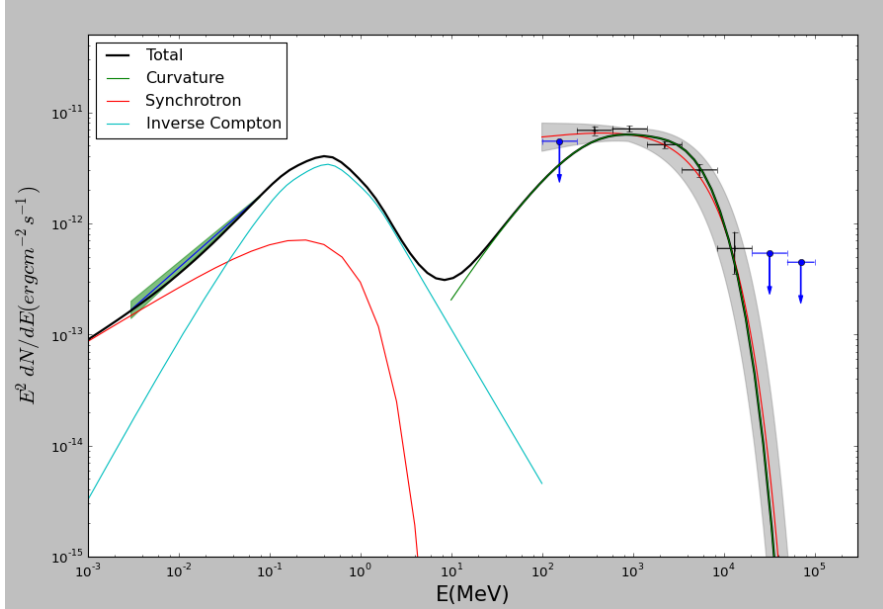


Figure 3.6: The broadband spectrum of PSR B1821-24. The meanings of grey shade and the green shade are the same as Figure 3.5.

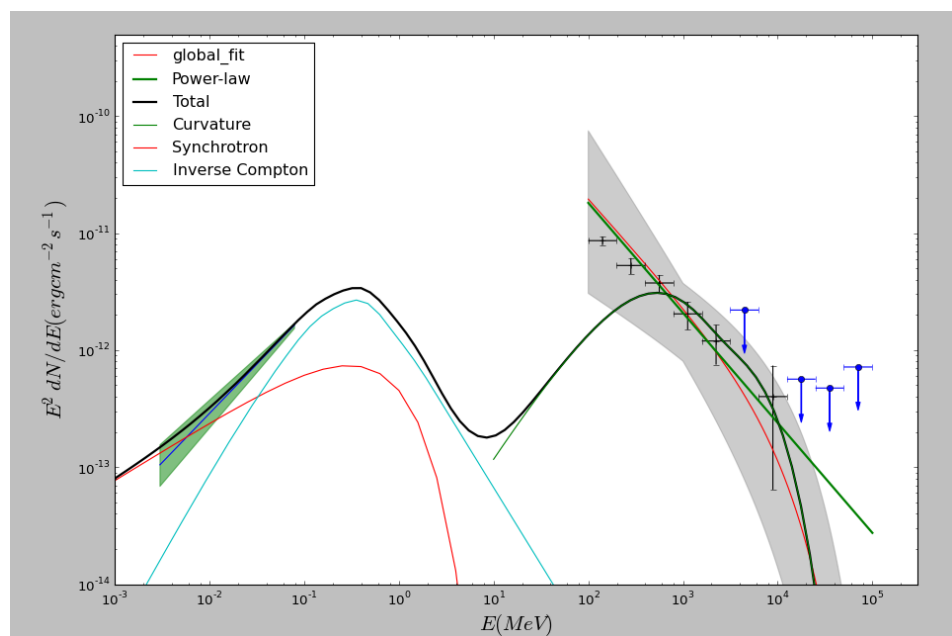


Figure 3.7: The broadband spectrum of PSR B1937+21. The meanings of grey shade and the green shade are the same as Figure 3.5.

Chapter 4

Discussion

The parameters f , g_1 , and h_1/h_2 have different impacts on the shapes of the gamma-ray spectra as Figures 4.1, 4.2, and 4.3 show. The parameter f controls the flux and cutoff energy (E_{cut}) of the spectra. Both the flux and E_{cut} increase with the increases of f . Moreover, this parameter has the most significant impacts on the shape of the spectra. The parameter g_1 mainly affects E_{cut} . Additionally, when g_1 is large enough (larger than 0.98), the shapes of the spectra becomes a little bit irregular. The parameter which has the strangest influences on the spectra is h_1/h_2 . As Figure 4.3 shows, the spectra are classified into two groups with different cutoff energies. In each group, h_1/h_2 has nearly no impact on E_{cut} . In addition, it also has small effects on the slopes of the spectra below E_{cut} . Like g_1 , if h_1/h_2 becomes too large, the shapes of the spectra are a little bit irregular. I have not found a convincing explanation yet and not sure if it reveals some emission properties or just numerical errors when the parameters become too extreme.

The patterns discussed above only apply to a particular pulsar. For instance, the values of f of PSRs J0218+4232 and B1821-24 are 0.330 and

0.247. Thus E_{cut} of PSR J0218+4232 should be larger than PSR B1821-24 because f has the most significant effects on the shapes of the spectra among the three parameters. However, E_{cut} is 3.77 ± 0.40 GeV for PSR J0218+4232 and 4.5 ± 0.71 GeV for PSR B1821-24, which is not consistent with the previous discussions. In addition, other pulsars does not follow the pattern neither as Table 4.1 shows. This may be because that the spectral properties are related to the sizes of light cylinders, magnetic fields at the light cylinders, inclination angles and many other properties of pulsars. The three parameters of the two-layer model describe the structure of the outer gap of a particular pulsar. Therefore, we may not get much information by comparing the three parameters between different pulsars.

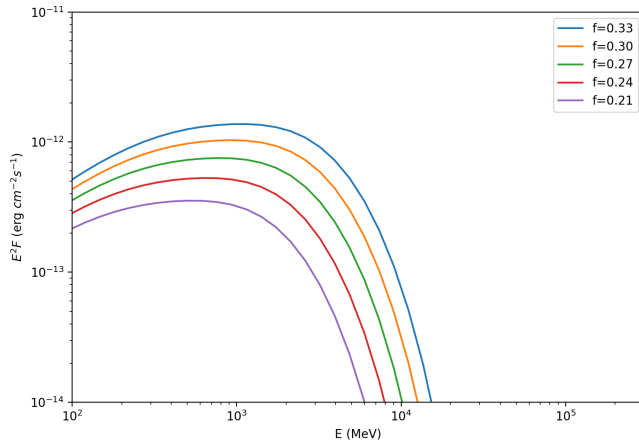


Figure 4.1: Effects of f on the shape of the gamma-ray spectrum. The parameters of PSR J0218+4232 are used. The other two parameters are $g_1 = 0.92$ and $h_1/h_2 = 0.915$.

4.1 Constraints of the Two-Layer Model

The simplified two-layer model is consistent with observational data to some extent. (The relevant data are reported by Wang et al. (2010)) The model uses four parameters to get a fairly good prediction of the gamma-ray spectra

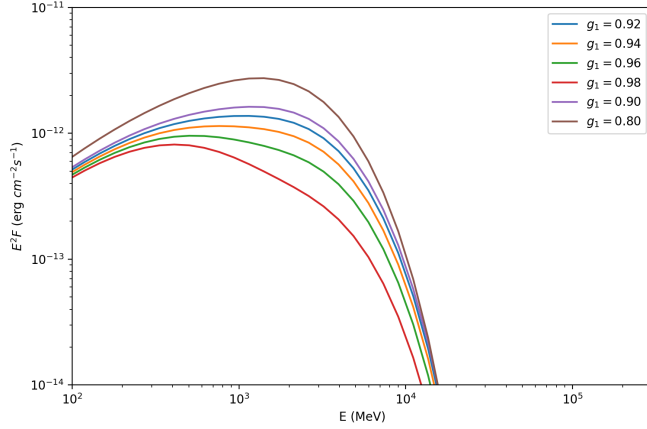


Figure 4.2: Effects of g_1 on the shape of the gamma-ray spectrum. The parameters of PSR J0218+4232 are used and $f = 0.33$, $h_1/h_2 = 0.915$.

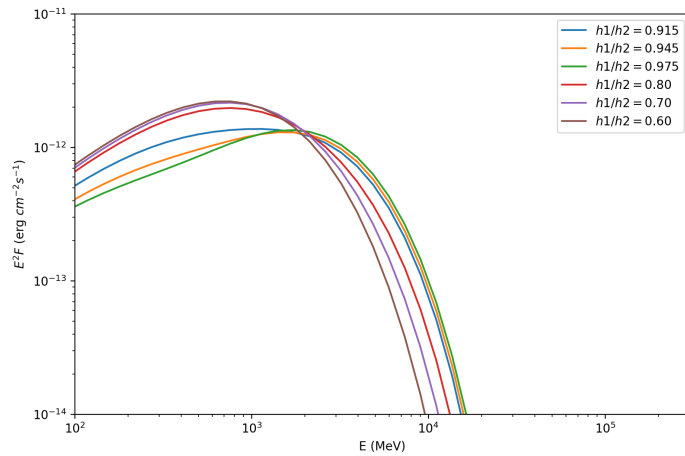


Figure 4.3: Effects of h_1/h_2 on the shape of the gamma-ray spectrum. The parameters of PSR J0218+4232 are used and $f = 0.33$, $g_1 = 0.92$.

Pulsar Name	P (ms)	f	g_1	h_1/h_2	E_{cut} (GeV)	Energy Flux (10^{-11} erg cm $^{-2}$ s $^{-1}$)
J0633+1746	237	0.76	0.85	0.933	2.2 ± 0.1	423.3 ± 1.2
J0835-4510	89.3	0.16	0.92	0.927	3.0 ± 0.1	906 ± 2
J0007+7303	316	0.65	0.94	0.967	4.7 ± 0.2	40 ± 0.4
J1057-5226	197	0.60	0.85	0.933	1.4 ± 0.1	29.5 ± 0.3
J0030+0451	4.9	0.60	0.88	0.947	1.8 ± 0.2	6.14 ± 0.18
J0437-4715	5.8	0.38	0.95	0.927	1.1 ± 0.3	1.67 ± 0.11

Table 4.1: The best-fit parameters of the two-layer model and observational properties for a few pulsars. Both young pulsars and MSPs are included.

of many pulsars. And all these four parameters have very obvious physical meanings. However, the problems of the model are clear — it is somewhat oversimplified. Although there are other more sophisticated versions of the two-layer model such as three-dimensional two-layer model (Wang et al. 2011) and I used the simpler one, which may cause some inconsistencies between the simulations and observations.

Therefore, we can briefly analyze which part is oversimplified and can be improved. First of all, we directly use a step function to describe the charged particle distribution. Though the charge density of the screening region is much larger than the primary region, using a step function is not very physical and may exaggerate the change rate of charge density. At the same time, the dramatic change of charge density also brings some numerical instabilities.

Secondly, the model sets the total of screening region and primary region to be rectangular. Though the actual shape is not clear, it should not be a rectangular in theory and may be very different. In the numerical simulation, changes in the shape of the regions will directly lead to a different integration

region, which may change the simulated spectra.

Thirdly, there are some inconsistencies in the model itself according to its assumptions. According to Equation 3.9 and Equation 3.10, since E'_{\parallel} can be 0, we know that γ_e can also be 0, which is absolutely non-physical. Although this may not have large influences on the spectra, it is the problem that should be avoided.

All in all, though the model has some constraints, it is very physical and the gamma-ray spectra computed based on the model is generally consistent with the observational data.

4.2 Inconsistency Between the Two-Layer Model and Fit Results

As Figures 3.5, 3.7, and 3.6 show, the two-layer model does not fit well for all three MSPs in the lower gamma-ray band (about 100 MeV), even though I have tried different reasonable parameter combinations. I think it is because the two-layer model used in the thesis is oversimplified. In most cases, the spectrum produced by the theoretical model is not monotonic and highly curved. However, the global fits of the PLEC model are usually very flat from 100MeV to 500MeV. This means that I can hardly reproduce the similar shape in this energy range, no matter what parameters I used. The fact that the gamma-ray emission predicted by the two-layer model is not as strong as the observational data in the energy range from 100MeV to 500MeV may also be explained by inverse-Compton radiation.

Chapter 5

Conclusion and Future Works

5.1 Conclusion

I do phase-averaged gamma-ray spectral analysis with about nine-year *Fermi* LAT data for PSRs J0218+4232, B1821-24 and B1937+21. The fit results are listed in Tables 2.9 and 2.10. The new results have smaller error bars thanks to Pass 8 dataset and much more observational data. Meanwhile, the TS values for PSRs J0218+4232 and B1821-24 are larger than previous studies as Table 2.9 shows. For PSR B1937+21, the power-law model is preferred since $TS_{cut} = 2\Delta \log(\text{likelihood}) = -2.86 < 9$ and I follow the convention in Abdo et al. (2013) like the previous study (Ng et al. 2014).

I also use the two-layer model to generate gamma-ray spectra for the three MSPs and obtain broadband spectra by combining inverse-Compton scattering and synchrotron radiation. The broadband spectra for the three MSPs are generally consistent with the observation in both hard X-rays and gamma-rays, except in a few hundred MeV energy range. Thus, it is reasonable to speculate that the radio and gamma-ray emission regions are co-located.

5.2 Analysis With LAT 8-year Point Source List

The latest preliminary LAT 8-year Point Source List (*FL8Y*) is released on May 03, 2018. Since the release date is a little bit late and the point source list is a preliminary version, I have not finished all the spectral analysis with the data. However, I would like to show some results I have done with the new source list together with my further plan.

Some spectra models are changed, for instance, the expression of PLSuperExpCutoff model has been changed as Equation 5.1 shows (J. Ballet & the Fermi-LAT collaboration 2018).

$$\frac{dN}{dE} = K \left(\frac{E}{E_0} \right)^\Gamma e^{(a(E_0^b - E^b))}. \quad (5.1)$$

Particularly, Fermi tools combine the E_0^b with K as Equation 5.2 shows and the model is renamed to PLSuperExpCutoff2.

$$\frac{dN}{dE} = K \left(\frac{E}{E_0} \right)^\Gamma e^{-aE^b}. \quad (5.2)$$

In principle, there is no difference between the Equations 2.4 and 5.2, however, the parameters needed to be fitted are different. The new point source list contains the source PSR B1937+21 and the default spectra model is PLEC2. However, the fit results for the MSP are still not easy to obtain. Table 5.1 lists the fit parameters for all the three MSPs.

The TS values for PSRs J0218+4232 and B1821-24 are both a little bit larger as Table 5.2 shows. Figures 5.1 and 5.2 are the fit spectra of the PSRs J0218+4232 and B1821-24. I still have not got a good fit result for PSR

	J0218+4232	B1821-24
Photon Index (Γ)	1.77 ± 0.07	1.14 ± 0.02
Expfactor (a, 10^{-3})	6.73 ± 0.86	11.76 ± 0.12
Scale (E_0)	821.48	1128.68
Index2 (b)	0.67	0.67
Photon Flux ($10^{-8} \text{ cm}^{-2}\text{s}^{-1}$)	7.44 ± 0.32	2.44 ± 0.08
Energy Flux ($10^{-11} \text{ erg cm}^{-2}\text{s}^{-1}$)	4.45 ± 0.16	2.08 ± 0.04
TS value	7189	980

Table 5.1: Fit results of PSRs J0218+4232 and B1821-24 with LAT 8-year Point Source List.

B1937+21 because this MSP takes more effort which is the same case as the 3FGL. Besides, the fit results for the two MSPs are also not the final results because I only have tried a few spectra models and have not compared the likelihood and TS values between different models.

Figures 5.3 and 5.4 are count spectra and count residuals plot for the two MSPs.

	J0218+4232	B1821-24
FL8Y	7189	980
3FGL	6809	941

Table 5.2: TS values comparison between 3FGL (older) and FL8Y (newer) source list.

5.3 Future Works

LAT 8-year Point Source List is only a preliminary list and 4FGL is being processed. I will continue to analyze the gamma-ray spectra of the three

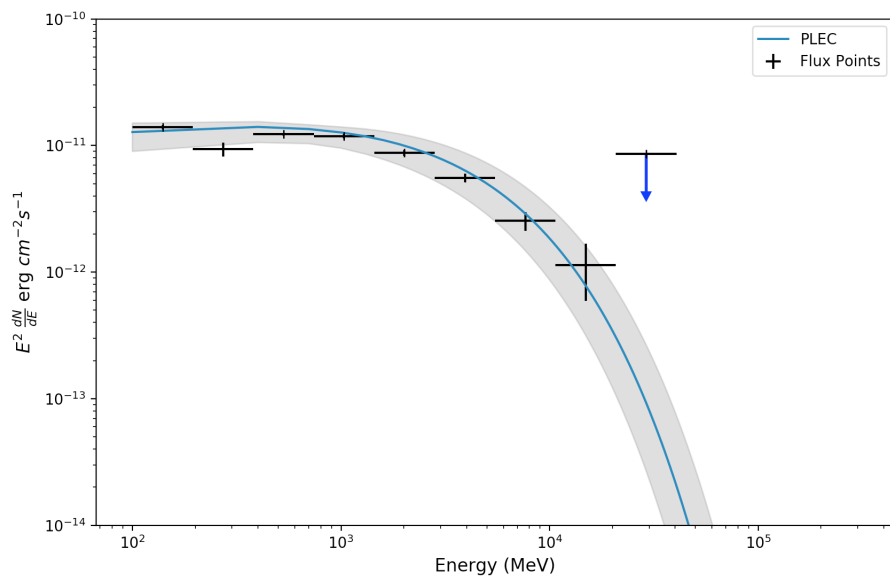


Figure 5.1: Gamma-ray spectra of PSR J0218+4232 with PLEC2 model.

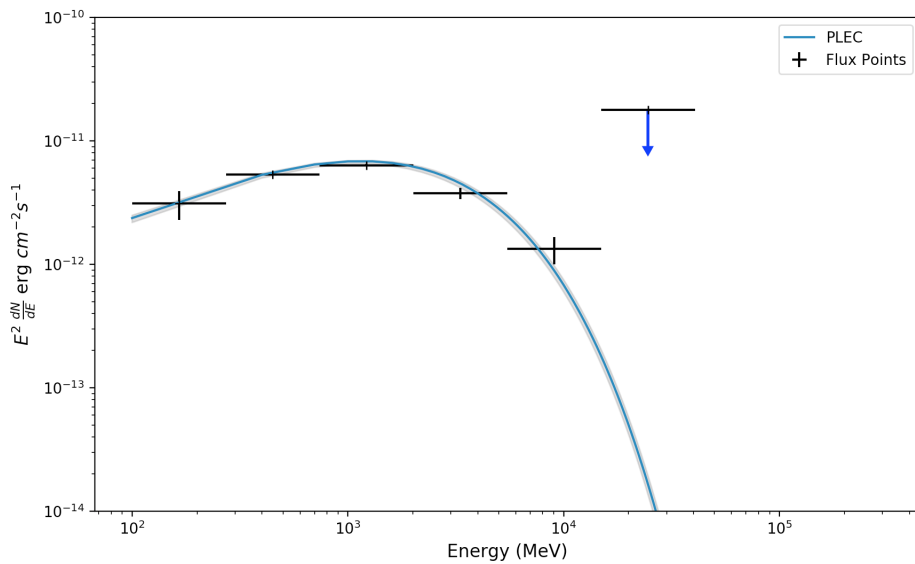


Figure 5.2: Gamma-ray spectra of PSR B1821-24 with PLEC2 model.

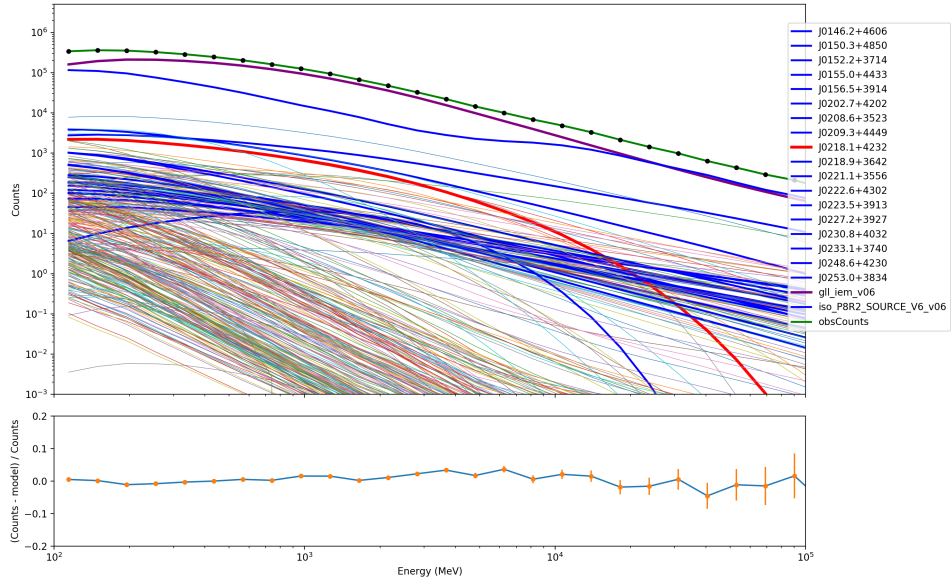


Figure 5.3: Count spectra and residuals of PSR J0218+4232

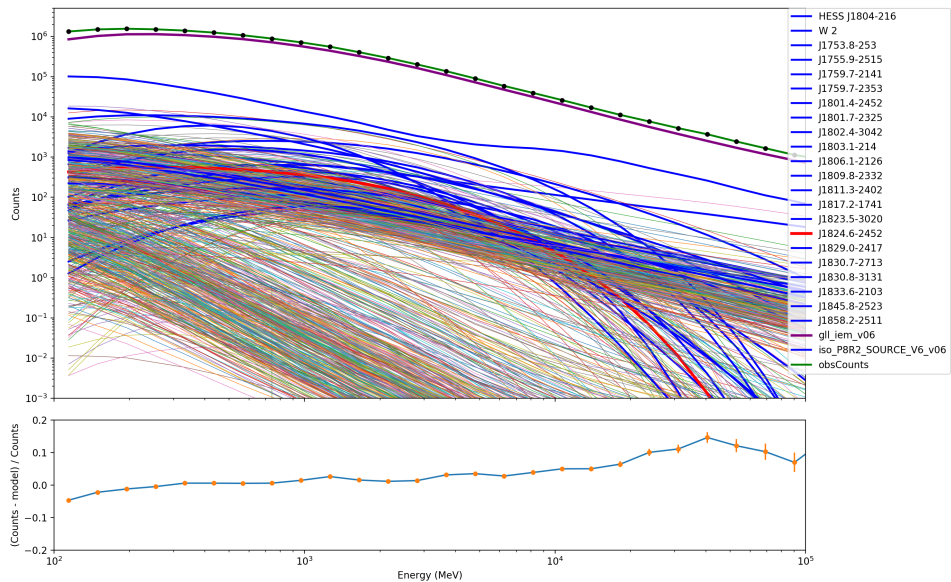


Figure 5.4: Count spectra and residuals of PSR B1821-24.

MSPs with the newer point source list in order to get more precise results. In addition, since *Fermi* LAT is producing large quantities of data, it is important to be able to handle the data effectively. I have created some pipeline scripts and am going to improve them, which can help me to study more pulsars with higher efficiency. Additionally, I am going to study the two-layer model more thoroughly and other emission models, then compare the predictions of the models with newer observational data.

Bibliography

- Abdo, A. A., Ajello, M., Allafort, A., et al. 2013, The Astrophysical Journal Supplement Series, 208, 17
- Backer, D. C., & et al., K. S. R. 1982, 300, 615
- Becker, W., Huang, H. H., & Prinz, T. 2010, ArXiv e-prints, arXiv:1006.0335
- Bogdanov, S., van den Berg, M., Servillat, M., et al. 2011, The Astrophysical Journal, 730, 81
- Cheng, K., Ho, C., & Ruderman, M. 1986, The Astrophysical Journal, 300, 500
- Cusumano, G., & et al., W. H. 2003, Astronomy & Astrophysics, 410, 9
- Goldreich, P., & Julian, W. H. 1969, The Astrophysical Journal, 157, 869
- Gotthelf, E. V., & Bogdanov, S. 2017, The Astrophysical Journal, 845, 159
- Guillemot, L., Johnson, T. J., & et al. 2012, doi:10.1088/0004-637X/744/1/33
- Hamil, O., Stone, J. R., Urbanec, M., & Urbancová, G. 2015, Phys. Rev. D, 91, 063007
- Huang, R. H. H., Kong, A. K. H., Takata, J., et al. 2012, The Astrophysical Journal, 760, 92
- J. Ballet, T. H. Burnett, B. L., & the Fermi-LAT collaboration. 2018

- Jenet, F. A., Creighton, T., & Lommen, A. 2005, *The Astrophysical Journal Letters*, 627, L125
- Johnson, T. J., Guillemot, L., I, M. K., et al. 2013, *The Astrophysics Journal*, 778, 106
- Kuiper, L., Hermsen, W., Verbunt, F., et al. 2002, *The Astrophysical Journal*, 577, 917
- Ng, C.-Y., Takata, J., Leung, G. C. K., Cheng, K. S., & Philippopoulos, P. 2014, *The Astrophysical Journal*, 787, 167
- Sturrock, P. A. 1971, *Astrophys. J.*, 164, 529
- Takata, J., Cheng, K. S., & Taam, R. E. 2012, *The Astrophysical Journal*, 745, 100
- Tong, H. 999, *Science China Physics, Mechanics Astronomy*, 59, 619501
- Verbunt, F., Kuiper, L., Hermsen, W., et al. 2003, 302, 355
- Wang, Y., Takata, J., & Cheng, K. S. 2010, *The Astrophysical Journal*, 720, 178
- . 2011, *Monthly Notices of the Royal Astronomical Society*, 414, 2664
- Webb, N. A., Olive, J.-F., & Barret, D. 2004, *Astronomy and Astrophysics*, 417, 181